TRANS-RECTAL OPTICAL TOMOGRAPHY RECONSTRUCTION USING 3-DIMENSIONAL SPATIAL PRIOR EXTRACTED FROM SPARSE 2-DIMENSIONAL TRANS-RECTAL ULTRASOUND IMAGERY

By

DHANASHREE PALANDE

Bachelor of Engineering in Electronics and

Telecommunication

University of Pune

India

2010

Submitted to the Faculty of the
Graduate College of the
Oklahoma State University
in partial fulfillment of
the requirements for
the Degree of
MASTER OF SCIENCE
July, 2013

TRANS-RECTAL OPTICAL TOMOGRAPHY RECONSTRUCTION USING 3-DIMENSIONAL SPATIAL PRIOR EXTRACTED FROM SPARSE 2-DIMENSIONAL TRANS-RECTAL ULTRASOUND IMAGERY

Thesis Approved:

Dr. Daqing Piao

Thesis Adviser

Dr. Martin Hagan

Dr. Guoliang Fan

ACKNOWLEDGEMENTS

I would firstly like to extend my greatest gratitude towards my adviser Dr. Daqing Piao for being the most dedicated and enthusiastic mentor. Without his accurate guidance and encouraging nature this work would not have been possible. I would like to take this opportunity to thank him for appointing me as a Research Assistant in his Optical Imaging Laboratory and introducing me to the world of medical imaging.

This work is dedicated to the memory of my grandmother Usha Marathe (1930-2012), a professor, who was a friend, a guide and a great role model in my life. She always inspired me to take up new challenges and achieve my goals in life. I would like to thank my parents Smita Palande and Shekhar Palande, Swati Mone and Tejaswini Palande for their encouragement, moral support and unconditional love during all the ups and downs experienced.

I am grateful to Dr. Hagan, who encouraged me to approach Dr. Piao, for I got this opportunity to explore the field of medical imaging

I would also like to thank the members of the Optical Imaging Laboratory for all the help they have provided in the completion of this work. Lastly, I thank my close friends for their support and best wishes.

Acknowledgements reflect the views of the author and are not endorsed by committee members or Oklahoma State University.

Name: DHANASHREE PALANDE

Date of Degree: JULY, 2013

Title of Study: TRANS-RECTAL OPTICAL TOMOGRAPHY RECONSTRUCTION USING 3-DIMENSIONAL SPATIAL PRIOR EXTRACTED FROM SPARSE 2-DIMENSIONAL TRANS-RECTAL ULTRASOUND IMAGERY

Major Field: ELECTRICAL ENGINEERING

Abstract:

Accurate prostate segmentation in trans-rectal ultrasound (TRUS) imagery is an important step in different clinical applications, and it is particularly necessary for providing a 3-dimensional spatial prior to guide the image reconstruction of trans-rectal optical tomography for prostate cancer detection. Utilizing the US *prior* to guide near infrared tomography reconstruction could be performed by direct segmentation of the US image. Therefore, 2-dimensional segmentation of the axial TRUS images are performed extensively, however, 2-dimensional segmentation of the sagittal TRUS images are challenging, due to more complexities in contrast, morphological features and image artifacts, as well as significant inter-subject variations of the prostate shape and size. We develop a routine of segmenting 2-dimensional TRUS images obtained from canine prostate, based on the combination of a Snake's algorithm and selected manual segmentation. The segmentations obtained from a sparse set of axial and sagittal images are aligned to form the 3-dimensional contour of a prostate. The resulted prostate profile is implemented as the spatial prior to constrain image reconstruction of trans-rectal optical tomography. The trans-rectal optical tomography images reconstructed with the prostate profile prior are compared with those reconstructed without any spatial prior by monitoring oxygen saturation (S_tO_2) and total hemoglobin concentration ([HbT]) in lesions of a canine prostate.

TABLE OF CONTENTS

Chapter Page

LIST OF TABLES

Table Page

LIST OF FIGURES

Figure Page

Figure Page

CHAPTER 1

INTRODUCTION

Prostate cancer (PCa) is one of the leading causes of death from cancer among men in the United States [1]. Rates of detection of prostate cancers vary widely across the world, with South and East Asia detecting less frequently than in Europe, and especially the United States [2]. Prostate cancer tends to develop in men over the age of fifty [3]. Globally, it is the sixth leading cause of cancer-related death in men [3]. Prostate cancer is most common in the developed world with increasing rates in the developing world [4].

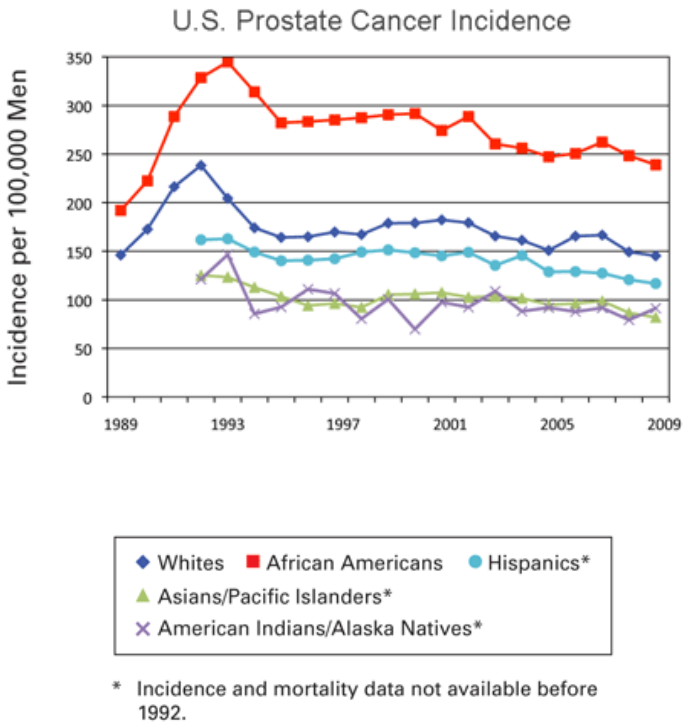

Figure 1.1 U.S. Prostate cancer incidences as of 2009

As per the National Cancer Institute, prostate cancer incidence rates rose dramatically in the late 1980s, when screening with the Prostate Specific Antigen (PSA) test, which received initial U.S. Food and Drug Administration approval in 1986, came into wide use. Since the early 1990s, prostate cancer incidence has been declining. Mortality rates for prostate cancer also have declined since the mid-1990s. Well-established risk factors for prostate cancer include increasing age, race, and a family history of prostate cancer. Current evidence suggests that screening with a digital rectal exam (DRE) and/or PSA has at most only a small effect on prostate cancer mortality. According to National Cancer Institute statistics, there are 238,590 new cases, 29,720 deaths due to prostate cancer and about 239,000 American men will be diagnosed with prostate cancer in 2013.

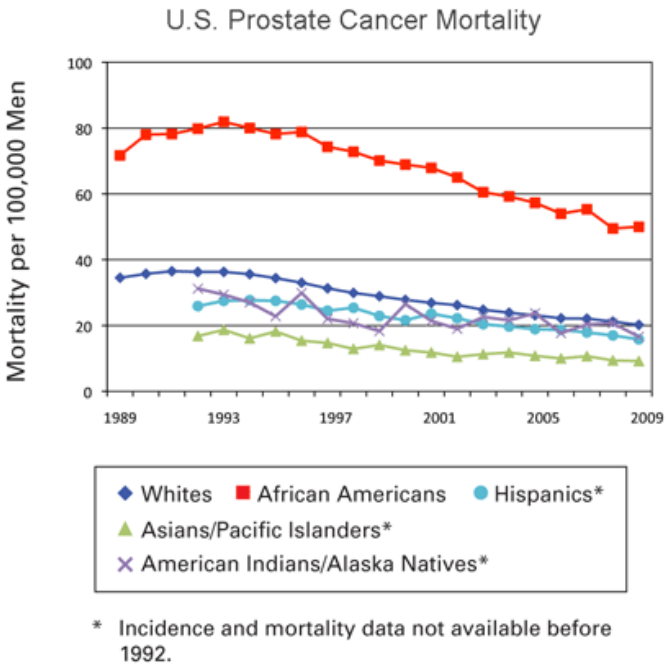

Source: Surveillance, Epidemiology, and End Results (SEER) Program and the National Center for Health Statistics. Additional statistics and charts are available at the SEER Web site.

Figure 1.2 U.S. Prostate cancer mortality as of 2009

1.1 Prostate

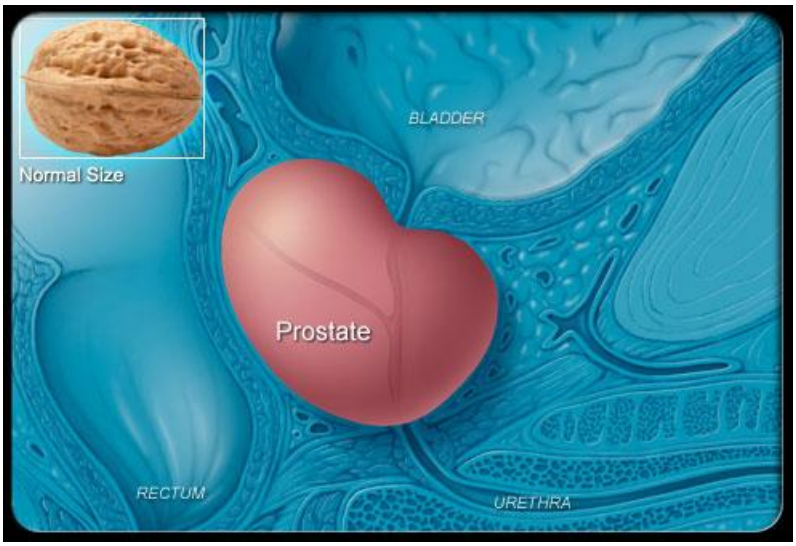

Figure 1.3 Prostate anatomy

The prostate is a small, walnut-sized structure that makes up part of a man's reproductive system. The prostate is a part of the male reproductive system that helps make and store seminal fluid. In adult men, a typical prostate is about three centimeters long and weighs about twenty grams [5]. It is located in the pelvis, under the urinary bladder and in front of the rectum [6]. It wraps around the urethra, the tube which carries urine out of the body. It is partly muscular and partly glandular, with ducts opening into the prostatic portion of the urethra. It is made up of three lobes: a center lobe with one lobe on each side.

The prostate gland has four distinct glandular regions, two of which arise from different segments of the prostatic urethra. They are as follows:

1) Peripheral zone (PZ): This is a sub-capsular portion of the posterior aspect of the prostate gland that surrounds the distal urethra. It is from this portion of the gland that ~70–80% of prostatic cancers originate.

2) Central zone (CZ): This zone surrounds the ejaculatory ducts. The central zone accounts for roughly 2.5% of prostate cancers although these cancers tend to be more aggressive and more likely to invade the seminal vesicles.

3) Transition zone (TZ): ~10–20% of prostate cancers originate in this zone. The transition zone surrounds the proximal urethra and is the region of the prostate gland that grows throughout life and is responsible for the disease of benign prostatic enlargement.

4) Anterior fibro-muscular zone (or stroma): This zone is usually devoid of glandular components, and composed only, as its name suggests, of muscle and fibrous tissue.

As part of the male reproductive system, the prostate gland's primary function is to make some of the fluid that protects and nourishes sperm cells in semen [7].

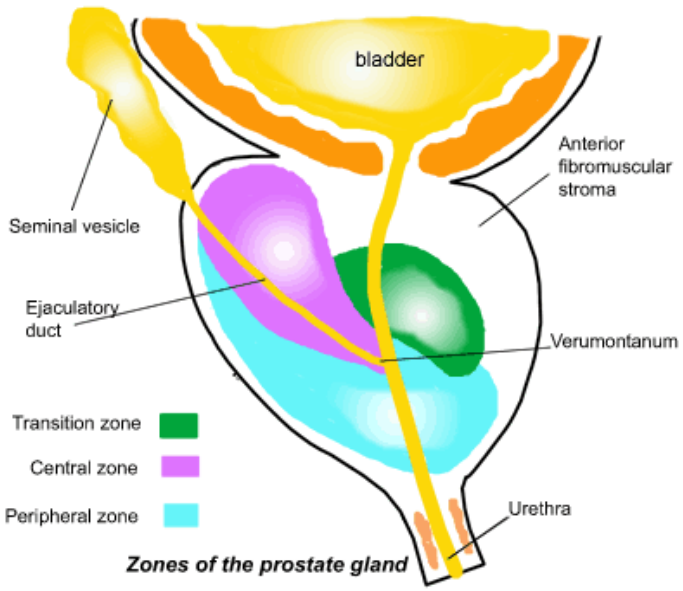

Figure 1.4 Zones of prostate gland

1.2 Prostate Cancer

Prostate cancer occurs when cells in the prostate gland grow out of control. The cancer cells may spread from the prostate to other parts of the body, particularly the bones and lymph nodes. Many prostate cancers grow slowly, and differentiating aggressive from indolent prostate cancer is an overarching challenge in prostate cancer study. There are 4 stages of prostate cancer.

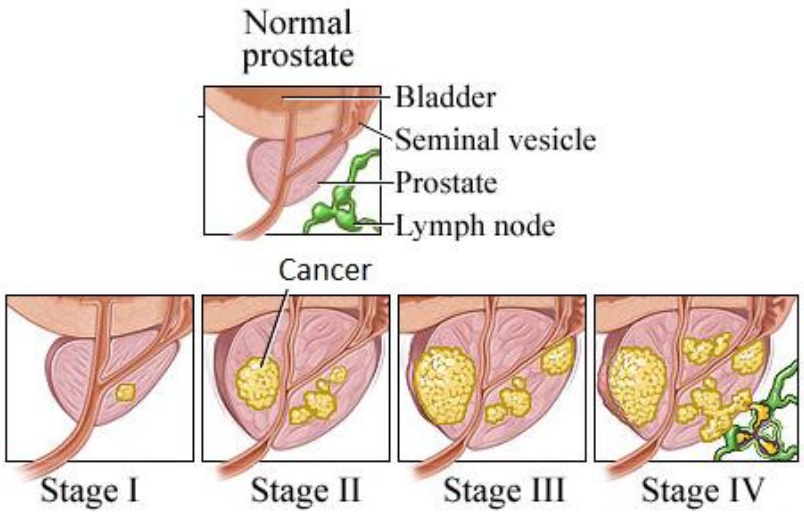

Figure 1.5 Stages of prostate cancer

Stage I. The cancer is only in the prostate. It might be too small to feel during a digital rectal exam. If the Gleason score and PSA level are known, the Gleason score is 6 or less, and the PSA level is under 10.

Stage II. The tumor is more advanced or a higher grade than Stage I, but the tumor does not extend beyond the prostate.

Stage III. The tumor extends beyond the prostate. The tumor may have invaded a seminal vesicle, but cancer cells have not spread to the lymph nodes.

Stage IV. The tumor may have invaded the bladder, rectum, or nearby structures (beyond the seminal vesicles). It may have spread to lymph nodes, bones, or other parts of the body.

There are often no early prostate cancer symptoms, but some men have urinary symptoms and discomfort. For prostate cancer identified as clinically significant (needing treatment), the treatment options are surgery, chemotherapy, cryotherapy, hormonal therapy, and/or radiation. In some instances, doctors recommend "watchful waiting."

1.3 TRUS Guided Near Infrared Optical Tomography

The need for more accurate imaging modalities, for both “targeted biopsy” and “targeted treatment,” have evoked investigation and development of a number of novel imaging technologies besides the standard modalities, such as Ultra Sound (US), Magnetic Resonance Imaging (MRI), and Computerized Tomography. Some of these novel approaches have emerged as alternative prostate imaging methods that provide new insights valuable in differentiating prostate cancer from benign tissues. Among these emerging alternative prostate imaging technologies, the approach using near-infrared (NIR) light has seemed to provide unique information regarding optical properties of the intact prostate that may be useful for detecting malignant tissue and pretreatment planning.

Recently, trans-rectal NIR imaging of the prostate has been investigated through simulation in the context of assisting MRI for a treatment decision [8]. Imaging methods which include US and MRI could provide reliable information about the size and shape of prostate gland and localize the cancer area to improve the accuracy of diagnosis and enabling more efficient treatment. Currently the most widely used modality for prostate cancer diagnosis is trans-rectal ultrasound (TRUS) because of its images. Trans-rectal probing is undoubtedly the most suitable way of prostate imaging for optical means. This probing option, however, indicates that trans-

rectal optical imaging may be combined with TRUS to provide broader clinical utility, e.g. prostate screening and biopsy guidance.

The benefit of complement NIR contrast to ultrasound has been demonstrated in breast imaging [9-10]. The methodology of combining NIR and US can certainly be extended from breast imaging to prostate imaging. The imaging modalities such as x-ray, ultrasound, and magnetic resonance imaging (MRI) provide higher imaging resolution but low functional contrast in biological tissue, which is opposite to optical diffuse imaging. Compensating optical imaging with spatial a priori information extracted from ultrasound imaging can potentially improve the specificity of DOT to malignant tissue. The pioneering works of ultrasound prior guided optical tomography reconstruction was conducted by an optical imaging group at the University of Connecticut.

1.4 Motivation and Objective

There is an interest in significant improvements in prostate cancer diagnosis and treatment. Researchers are trying to determine the best way to screen for this type of prostate cancer because it is a relatively unknown and rare type of prostate cancer but very serious and quick to spread to other parts of the body. Trans-rectal optical tomography (DOT) has the potential to non-invasively reveal optical signatures of prostatic lesions. Different tissue types often have distinct scattering properties, and thereby, we can hope to image this distinction as well. Thus, NIR methods have the potential to provide *in vivo* hemoglobin imaging as a noninvasive assessment of blood/vascular status in tissue. This approach was motivated by the hypothesis that optical properties of prostate cancer in vivo may be different from those of normal intact prostate tissues and was challenged by the difficulty of assessing the prostate in its in vivo real-time environment [11]. The main disadvantage of NIR tomography lies in the low spatial resolution resulting from the highly scattering nature of tissue for these wavelengths.

Since trans-rectal ultrasound is widely used in prostate cancer diagnosis and prostate biopsy guidance, we use axial and sagittal trans-rectal ultrasound images of a prostate for structural prior extraction. Utilizing the US prior to guide NIR tomography reconstruction could be performed by direct segmentation of the US image. Hence, our objective is to develop a routine of segmenting TRUS images obtained from a canine prostate, based on the combination of a Snake algorithm and selected manual segmentation. The segmentations obtained from a sparse set of axial and sagittal images are aligned to form the 3-dimensional contour of a prostate. This 3-D contour provided by TRUS imaging will be used as the spatial structural prior in trans-rectal optical tomography reconstruction to improve the image reconstruction outcome of TR-NIR.

1.5 Organization of Thesis

The remainder of thesis is organized as follows: A literature review is presented in chapter 2. Chapter 3 explains the methodology for 3-D profiling of a canine prostate. Optical tomography reconstruction using NIRFAST is shown in chapter 4. Chapter 5 provides results and discussion from the study. Conclusion and future work are given in chapter 6.

CHAPTER 2

LITERATURE REVIEW

2.1 PROSTATE CANCER DIAGNOSIS

Prostate cancer screening involves testing for prostate cancer in men who have no symptoms of the disease. This testing can find cancer at an early stage. However, medical experts disagree about whether prostate cancer screening is right for all men, and it is not clear if the benefits of screening outweigh the risks. The diagnosis procedure involves tests like PSA and DRE. If the test results are not normal, there is a possibility of prostate cancer. If the reports of the tests are normal, still it does not rule out the suspicion of prostate cancer. Therefore, it is recommended to repeat the tests again.

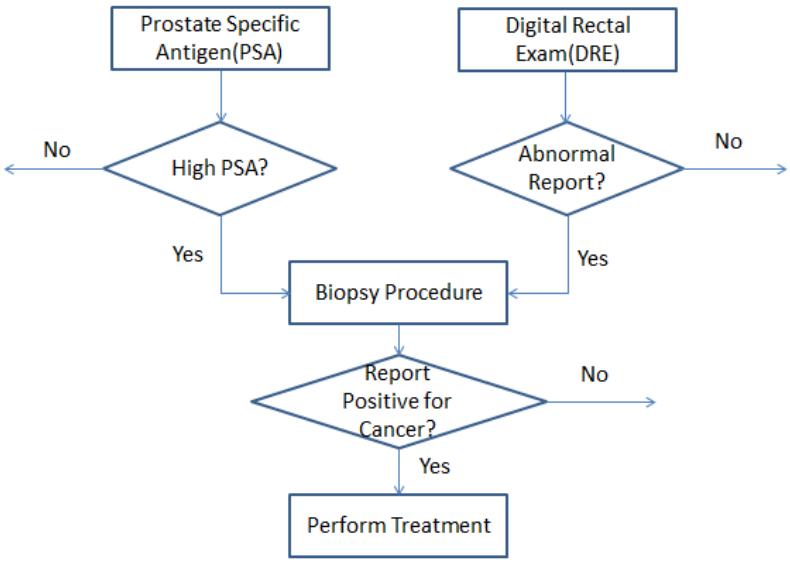

Figure 2.1 Prostate cancer diagnosis procedure

2.1.1 Tests Available for Prostate Cancer Screening

Prostate cancer screening is an attempt to identify individuals with prostate cancer in a broad segment of the population, those for whom there is no reason to suspect prostate cancer. The screening of prostate cancer currently involves determination of prostate-specific antigen (PSA) and digital rectal examination (DRE), recommended to begin at 50 years of age for men with general risk or at 40 years of age for men with high risk, such as individuals having a family history of prostate cancer [12]. If PSA or DRE reports are abnormal, it leads to suspicion of cancer and biopsy is performed by the doctors.

2.1.1.1 Prostate-specific antigen (PSA) blood test

Prostate-specific antigen, or PSA, is a protein produced by cells of the prostate gland. The PSA test measures the level of PSA in a man's blood. For this test, a blood sample is sent to a laboratory for analysis. The results are usually reported as nano grams of PSA per milliliter (ng/mL) of blood. The chance of having prostate cancer goes up as the PSA level goes up. There is no specific normal or abnormal level of PSA in the blood. In the past, most doctors considered PSA levels of 4.0 ng/mL and lower as normal. However, as per the National Cancer Institute, more recent studies have shown that some men with PSA levels below 4.0 ng/mL have prostate cancer and that many men with higher levels do not have prostate cancer. If the PSA level is high, a doctor may advise either waiting a while or repeating the test, or getting a prostate biopsy to find out if the person has cancer. Not all doctors use the same PSA cutoff point when advising whether to do a biopsy. Some may advise it if the PSA is 4.0 ng/mL or higher, while others might recommend it at 2.5 ng/mL or higher. Other factors, such as age, race, and family history, may also come into play.

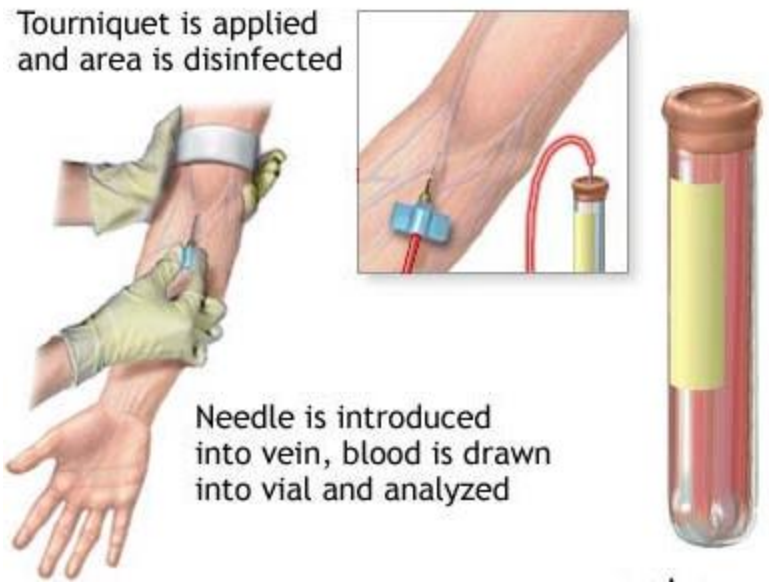

Figure 2.2 Prostate specific antigen (PSA) test

PSA tests are not foolproof. It's possible for PSA levels to be elevated when cancer is not present, and to not be elevated when cancer is present. Hence, false reassurance from a PSA test that does not reveal cancer (false-negative), leading to a missed diagnosis of aggressive prostate cancer that needs treatment makes PSA controversial.

2.1.1.2 Digital rectal exam (DRE)

For a digital rectal exam (DRE), the doctor inserts a gloved, lubricated finger into the rectum to feel for any bumps or hard areas on the prostate that might be cancer. Most cancers begin in the back part of the gland, which can be felt during a rectal exam. This exam can be uncomfortable, but it usually is not painful and only takes a short time.

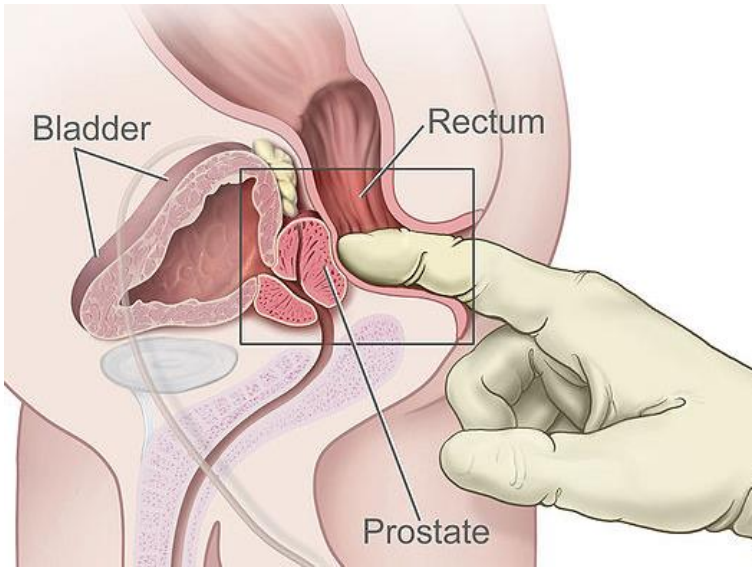

Figure 2.3 Digital rectal exam

DRE is less effective than the PSA blood test in finding prostate cancer, but it can sometimes find cancers in men with normal PSA levels. For this reason, it may be included as a part of prostate cancer screening.

2.1.1.3 Biopsy

A biopsy is when the doctor takes out tiny pieces of the prostate gland with a needle. The pieces are examined under a microscope to look for cancer cells. Directed biopsies are obtained from any area that is considered suggestive on the basis of ultra-sonographic findings or palpable abnormalities found on the digital rectal examination (DRE). Because the incidence of non-palpable iso-echoic prostate tumors is high, limiting biopsy sites to either ultra-sonographically hypo-echoic lesions or to areas of palpable abnormality tends doctors to miss many malignancies. Obtaining separate biopsy samples from each sextant of the prostate improves the odds of sampling clinically unapparent tumors. Originally, these biopsy sites included the mid-lobe parasagittal plane at the apex, the mid-gland, and the base bilaterally. Subsequently, however, changes to this protocol were recommended.

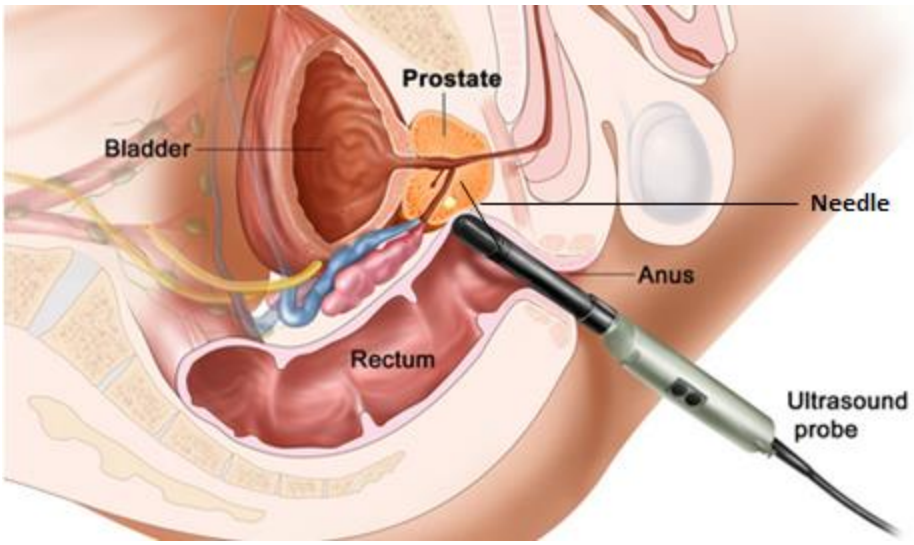

Figure 2.4 TRUS guided prostate biopsy

If the biopsy shows prostate cancer, the lab gives it a Gleason score. Gleason scores range from 2 to 10. They give an idea of how fast the cancer may grow. A lower Gleason score (2 to 5) means the cancer is slower to grow. A higher score (8 to 10) means the cancer is more "aggressive" and more likely to spread. Most men with prostate cancer have a score in the middle (6 to 7). Surviving prostate cancer is more likely with lower Gleason scores. This is true with any prostate cancer treatment or watchful waiting.

2.1.2 Prostate Cancer Screening Using MRI and TRUS Imagery

As mentioned in the introduction, different modalities like CT, MRI and TRUS are used for prostate imaging which can help detect the PCa. MRI scans can be helpful in looking at prostate cancer. They can produce a very clear picture of the prostate and show whether the cancer has spread outside the prostate into the seminal vesicles or other nearby structures. This information can be very important for doctors in planning the treatment. However, MRI scans may not provide useful information about newly diagnosed prostate cancers that are likely to be confined to the prostate based on other factors.

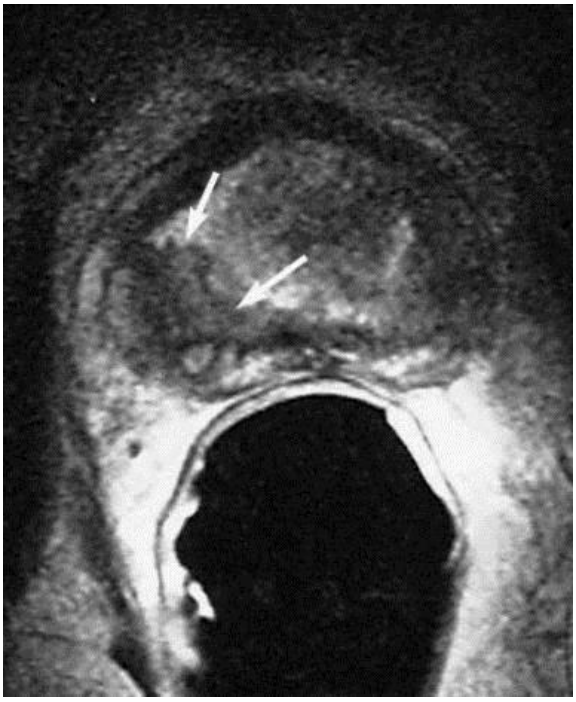

Figure 2.5 Magnetic resonance imaging (MRI) scan in a patient with a prostate-specific antigen level of 8 ng/mL and right-sided prostate cancer. Low signal intensity is demonstrated in the right peripheral zone (arrow).

Urologists have incorporated trans-rectal ultrasonography (TRUS) of the prostate into their practices. Trans-rectal ultrasound (TRUS) uses sound waves to make an image of the prostate on a video screen. For this test, a small probe that gives off sound waves is placed into the rectum. The sound waves enter the prostate and create echoes that are picked up by the probe. A computer turns the pattern of echoes into a black and white image of the prostate. TRUS may be used on its own to look at the prostate, but it is most often used during a prostate biopsy to guide the needles into the right area of the prostate. However, it was not found to be highly effective for this purpose of detecting prostate cancer, because of its lack of specificity: prostate cancer lesions may appear hypoechoic, hyperechoic, or isoechoic on the TRUS images.

TRUS images

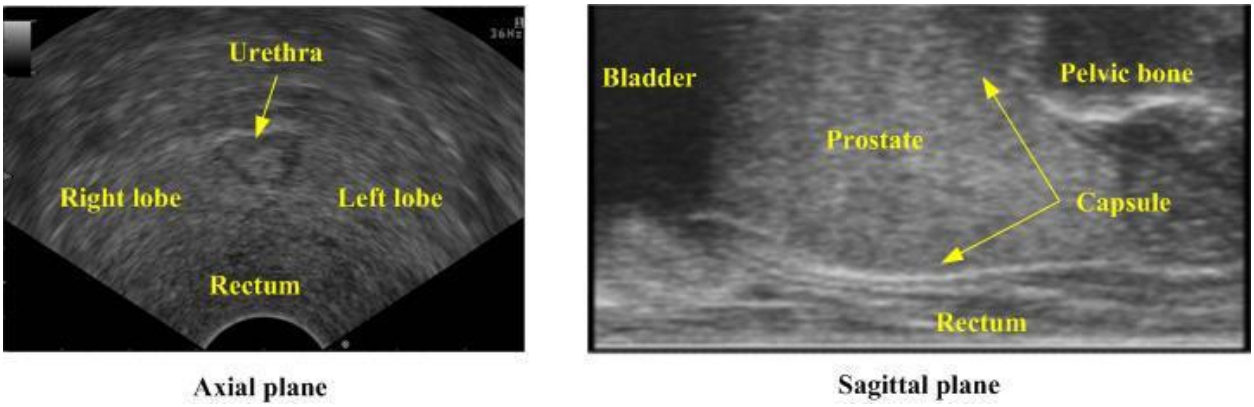

Figure 2.6 TRUS of prostate in axial and sagittal planes

The convention for presenting ultrasound images in longitudinal view puts the patient's head to the left and his feet to the right. In the clinical axial plane imaging, the left side of the image actually indicates the prostate right lobe; the right side of the image shows the left lobe of the prostate. Fig. 2.6 shows the axial and sagittal ultrasound of the canine prostate. The prostate region can be well defined by the capsule line shown in the ultrasound image. In the sagittal plane image, the bladder and pelvic bones can also be used to correlate the location of the prostate with respect to the probe since the bladder has a clear hypo-echoic region and the pelvic bone has a distinct hyper-echoic region in US images.

The Institutional Animal Care and Use Committee of Oklahoma State University approved this study. An adult 27-kg, intact male, foxhound estimated to be seven years of age was used. The trans-rectal US-integrated triple-band spectral optical tomography system used was developed based on an Aloka® trans-rectal ultrasound unit.

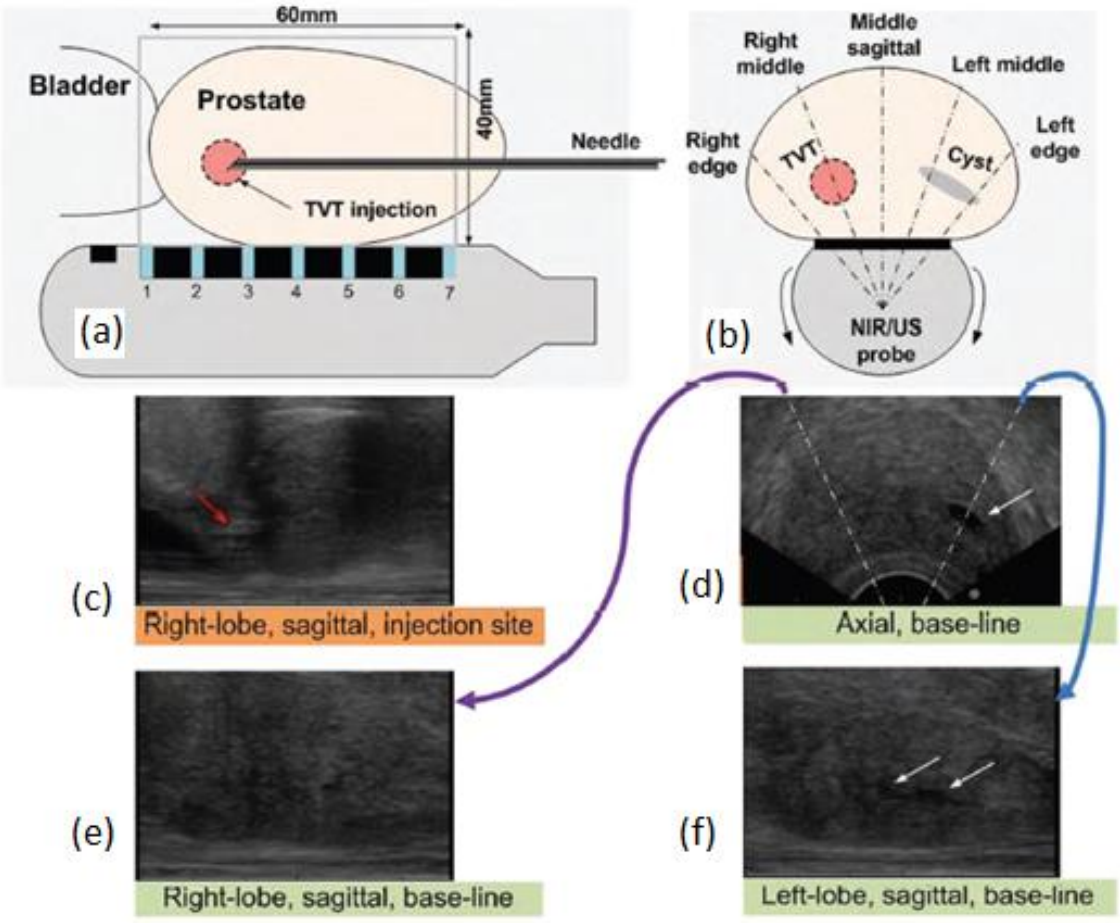

Figure 2.7 The study was conducted on a dog that had a naturally occurring cystic lesion in its left lobe. Order of sub-figures: clockwise from the upper-left. (a) and (b), imaging geometry; (d) and (f), a large "scorpion-like" cystic lesion extending irregularly within the left lobe; (e), the right lobe was unremarkable on the base-line US; (c), the TVT injection site in the right lobe was noticeable on US as indicated by the red arrow. White solid arrow: cystic lesion.

For all baseline and post-injection examinations, trans-rectal US-integrated optical tomography was performed on five quasi-sagittal planes (Fig. 2.7 b), including the middle-

sagittal, half-way to the right lateral edge, the right lateral edge, half-way to the left lateral edge, and the left lateral edge of the prostate gland for "laterality" evaluation. On each of the five quasi-sagittal planes the imaging was performed at three longitudinal positions of the optical-array probe with respect to the prostate. For the case of the middle-sagittal plane, at the longitudinal position 1 the imaging field-of-view covered the cranial edge of the prostate with the bladder visible, at the longitudinal position 3 the imaging field-of-view covered the caudal edge of the prostate, and the longitudinal position 2 was in between the longitudinal positions 1 and 3. Such measurements were necessary for cross-validation of the NIR imaging features associated with each quasi-sagittal plane.

Urologists use trans-rectal ultrasound during a prostate biopsy and can sometimes see a hypo-echoic area which are tissues or structures that reflect relatively less of the ultrasound waves directed at them. Fig 2.8 shows axial and sagittal views of a canine prostate with the hypo-echoic tumor lesions marked with white arrows.

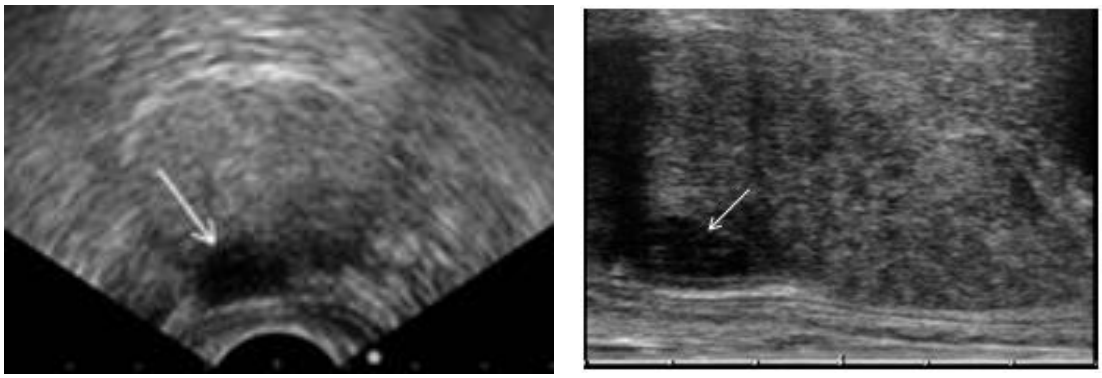

(a) (b)

Figure 2.8 (a) Large hypo-echoic area along the right peripheral zone, suggestive of carcinoma in axial view, (b) Sagittal image of the prostate showing a hypo-echoic area (white arrow).

2.2 Near-Infrared Optical Tomography

Near Infrared (NIR) optical imaging is a technique where NIR light (650–900 nm) is injected through optical fibers positioned on the surface of the imaging volume of interest and the emergent light is measured at other locations on the same tissue surface using either other fibers or a detector array[13]. It is a non-invasive imaging technique that aims to reconstruct images of tissue function and physiology, for the detection and characterization of malignant tumor. NIRS was used to provide the changes in the mean concentration of chromophores in the volume sampled by a source and detector pair, or a topological map if multiple pairs were used [14]. Until the recent decade, with the development in modeling of light propagation in tissue and the current detection technology, it is possible to combine NIR spectroscopy with tomography to perform diffuse optical tomography (DOT) which can spatially resolve the distribution of chromophore concentrations and scattering properties within the volume imaged.

The basic idea is that light is applied to the surface of the tissue, by the use of optical fibers, and the measured intensity and path-length of the out-coming light from other surface mounted fibers are used, together with a model based reconstruction algorithm to produce images of the internal light attenuation μ_a and reduced scatter μ_s' coefficient distribution. NIR optical tomography is also referred to as diffuse optical tomography.

Biological tissue is highly scattering at NIR wavelengths, and it can be observed from Fig. 2.9 that in the range of 700-900nm, the absorption of water is much lower than that of oxygenated hemoglobin and deoxygenated hemoglobin. Both features ensure considerable penetration depths and the possibility of measuring tissue oxygen saturation level with Near-infrared light. With such theoretical basis and assuming homogeneity in biological tissue, Near-infrared optical spectroscopy has been developed to monitor the hemoglobin concentration and oxygen saturation in human tissue with a single source-detector pair. Subsequently, it is

demonstrated that with multiple measurements, the heterogeneities of the hemoglobin concentration and oxygen saturation level can actually be resolved, which extends the spectroscopy system to a tomography system [15].

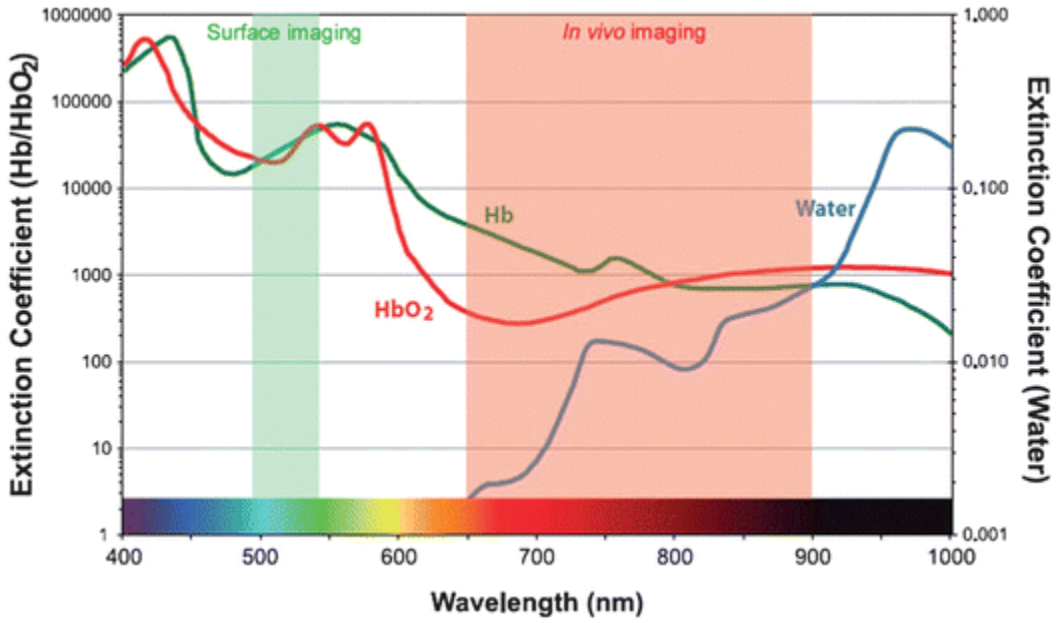

Figure 2.9 Absorption spectrum of human tissue in near-infrared band

The method is successfully implemented in imaging applications such as the diagnosis of breast and prostate cancer, the analysis of premature infant brain activities, and imaging of small animals as optical contrast generated by the functional variation of the biological tissue is sufficiently high for near-infrared light. However, since scattering dominates the photon propagation in biological tissue in the near-infrared band, the resolution of NIR tomography is relatively low.

NIR measurements of attenuation through tissue have demonstrated significant contrast gradients between blood and parenchymal tissue that is otherwise difficult to obtain [8, 16-20]. The alteration of vascularity or the hemoglobin content in the tumor renders high intrinsic optical

contrast between the tumor and benign tissues. This high NIR tumor-tissue contrast has been well-demonstrated in functional imaging of breast cancer [8, 16-20]. When multi-spectral detection is engaged, NIR imaging is also known for direct quantification of chromophore concentration that is important for characterization of the malignancy [8, 16-20]. For a prostate, studies have shown vascular density gradient in malignant versus benign tissue specimens [21], and different water concentrations in cancerous and benign tissues in vitro [22]. Invasive NIR measurements of a prostate have been reported for experimental prostate tumors [23] and human prostate [24-25]. Surface measurements of implanted prostate tumors have also been conducted [24, 26-27]. These studies have been based on using NIR to detect the prostate cancer. In fact, NIR diffuse optical measurement, performed interstitially, is becoming an important tool for monitoring photodynamic therapy in prostate [24-25]. Non-invasive NIR imaging of the prostate has also been analyzed and attempted via trans-urethral probing [28].

For many solid tumors, including tumors in the prostate, hypoxia has been correlated with angiogenesis [29], tumor aggressiveness [30] local recurrence [31], and metastasis [32]. Hypoxia also appears to be a prognostic factor in prostate cancer [33, 34]. The relationship between prostate tumor oxygenation and response to radiation therapy has been well established [35], but hypoxia also affects and is affected by some chemotherapeutic agents [36]. Although hypoxia is an important aspect of tumor physiology and response to treatment, the lack of simple and efficient methods to image oxygenation hampers further understanding and limits their prognostic usefulness [37]. There is no ‘gold standard’ for hypoxia measurement [38]. Many noninvasive imaging technologies currently in clinical use rely on expensive equipment, and measurement of secreted markers provides an indirect measurement of hypoxia [37].

2.3 Reconstruction Enhancement With Spatial Prior

The main disadvantage of near-infrared tomography lies in the low spatial resolution resulting from the highly scattering nature of tissue for these wavelengths. Studies have shown that

anatomical information from other modalities such as MRI or ultrasound, when used in the reconstruction procedure, can improve the stability of the reconstruction. A combined trans-rectal ultrasound and near-infrared (TR-NIR) imaging modality can potentially yield high resolution maps of optical properties from noninvasive simultaneous measurement. Therefore, to improve the spatial resolution of DOT, structural spatial prior obtained from other modalities can be used.

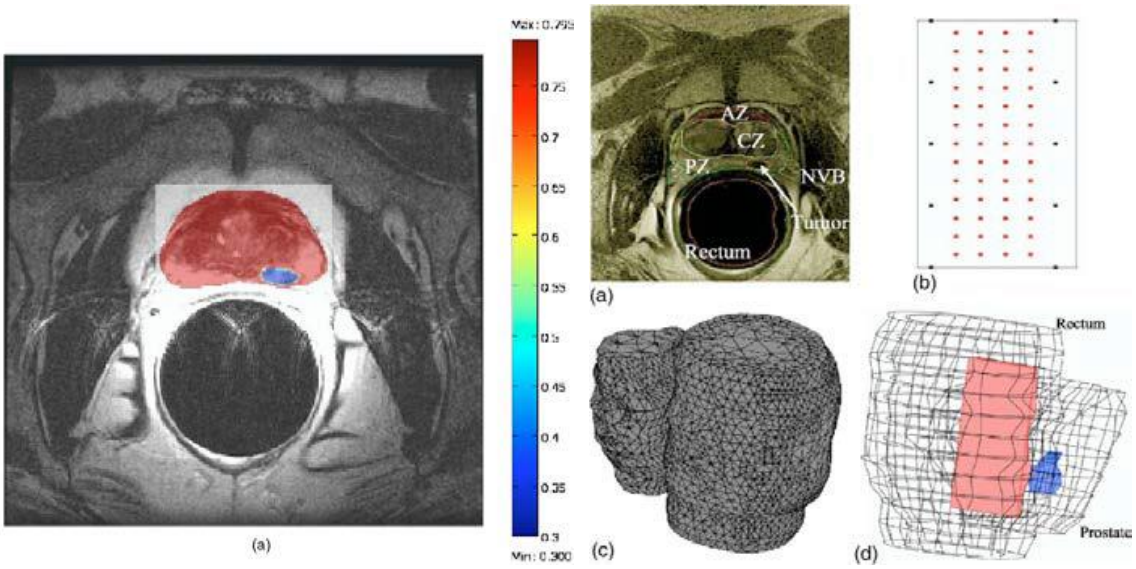

Figure 2.10 MRI a priori information utilization in NIR tomography on prostate

Fig. 2.10 [39] shows the MRI spatial prior information used to get a 3-D profile which is used as a structural spatial prior for NIR tomography of a prostate. Pogue et al. [40] tested such an algorithm in a case study of the optical changes in a rat cranium in response to variations in inhaled oxygen. They created a mesh from the MRI of the rat cranium, which provides a good estimate of the actual shape of the tissue boundary. Further, they segmented their mesh and assigned relevant optical properties (from the literature) to each tissue region as an initial guess. Their image reconstruction process refined these values either spatially throughout the image, or in terms of the segmented homogeneous tissue region values. They used knowledge of the

structure to apply reasonable constraints to the NIR image reconstruction algorithm, such as not allowing the optical properties in the bone region to exceed physiologically relevant values.

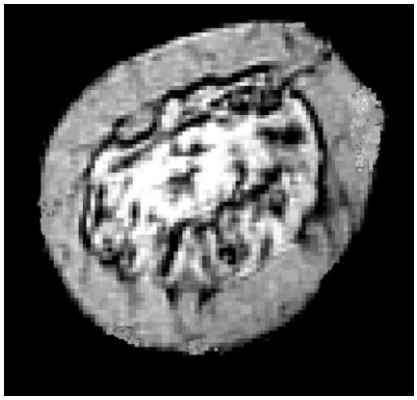

(a)

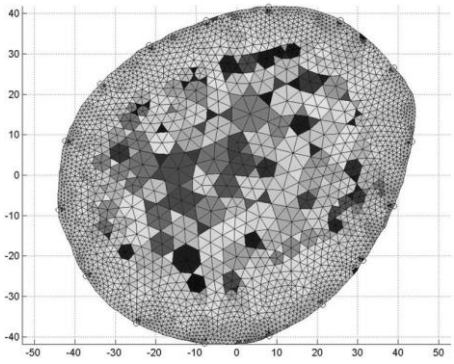

(b)

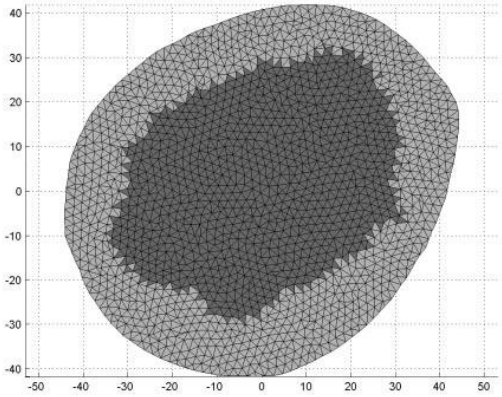

(c)

Figure 2.11 (a) Coronal slices MRI of a healthy female breast midway between the chest and the nipple. Adipose tissue (on periphery) and heterogeneous glandular tissue (interior) regions are clearly visible. (b) Finite element breast mesh with spatial heterogeneity in optical properties, modeled after heterogeneity patterns observed in the MRI (c) Mesh segmented into two regions; one corresponds to glandular tissue (interior region) and the

other corresponds to adipose tissue (exterior region). This region segmentation is used to assist and constrain reconstruction.

Fig. 2.11 [41] shows MRI spatial prior information extraction and its integration into geometry generation and region division of finite element meshes.

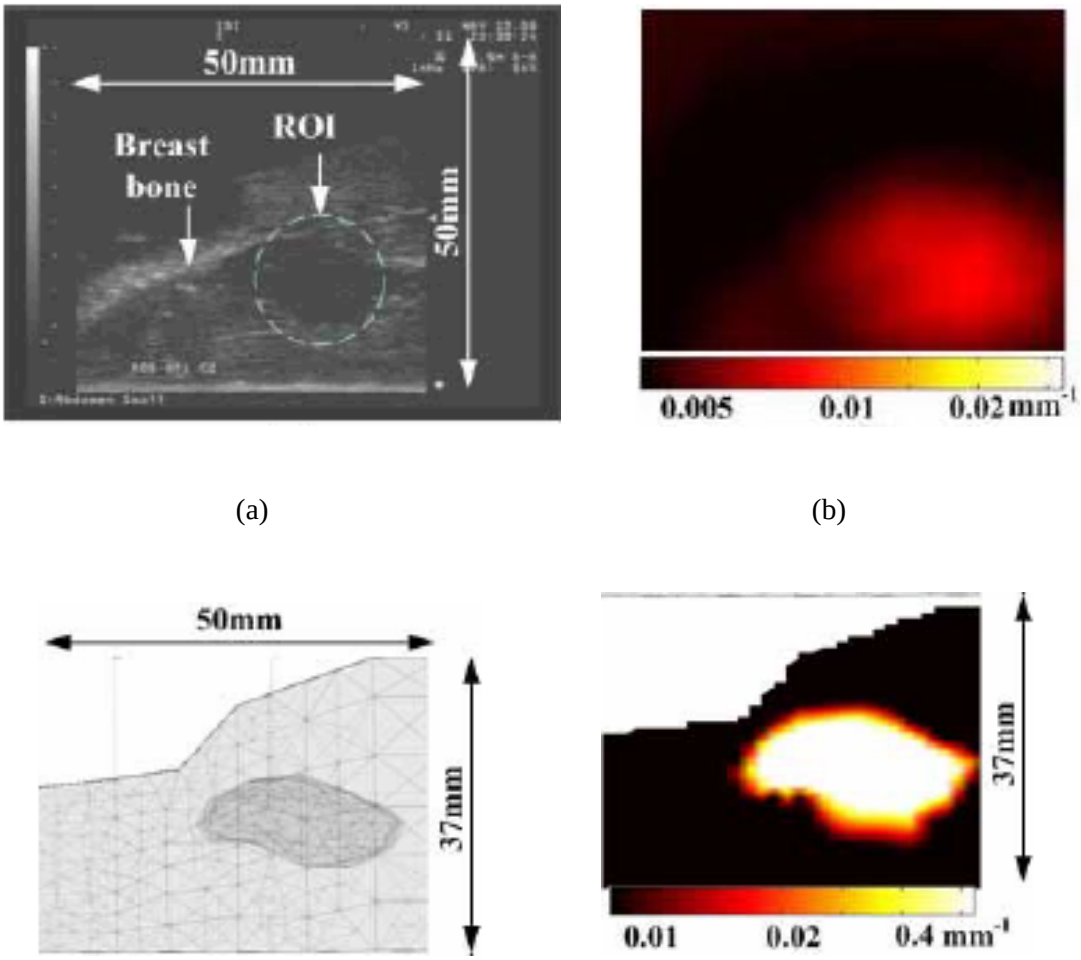

Figure 2.12 (a) US image of the embedded liver tissue (b) NIR image reconstructed without US prior,(c) Added boundary profile of background tissue, (d) NIR image reconstructed by adding the boundary profile of the background tissue

Literature in [42] shows that the accuracy of reconstruction for a highly heterogeneous domain can be improved dramatically by use of the TRUS spatial prior. Implementing frequency-domain detection to the NIR system will also allow more accurate reconstruction of the absorption coefficient owing to the reliable differentiation of it from the scattering by true phase information. Fig. 2.12 delivers the results discussed in the paper.

The application of spatial prior is not limited to FEM generation but also contribute to inverse problem regularization. There are two categories of methods, hard and soft prior integration to reconstruction algorithms are practiced and discussed in several literatures [43]. The hard prior method basically divides the imaging volume into several regions according to the contours observed from the prior providing image and assumes optical property homogeneity within each region. This method substantially reduced the unknown optical properties values compared to traditional reconstruction methods (number of regions versus number of nodes in FEM mesh) and generate high optical property recovery accuracy. Whereas the soft prior method still reconstructs the optical properties of each node of the FEM mesh. The update ratio of the suspected region is intentionally elevated, producing weighted sensitivity distribution and improving the reconstruction reliability [43]. However, the structural prior method will not be applicable for occasions where the malignant tissue cannot be visibly segmented.

2.4 Prostate Image Segmentation

The imaging modalities such as ultrasound and magnetic resonance imaging (MRI) provide higher imaging resolution but low functional contrast in biological tissue, which is opposite to optical diffuse imaging. Compensating optical imaging with spatial *a priori* information extracted from ultrasound or MRI imaging can potentially improve the specificity of DOT to malignant tissue.

TRUS and MRI provide information about the size and shape of the prostate. With their increased utilization, the number of TRUS and MRI systems and the number of radiologists and urologists performing TRUS and MRI has greatly increased. Nevertheless, there is still a great deal of controversy about the role of the ultrasound in the diagnosis and staging of prostate cancer. Use of ultrasound imaging has become widely spread because of its ability to visualize main organs with no injurious effects. Extraction of useful features from the segmented structure is crucial for automated diagnosis and staging of prostate cancer. Feature extraction simply means to pull out useful measures from the segmented structure. These measures are possibly based on a mathematical statistical foundation of the segmented structure or it may have physical meaning like the volume of the prostate itself.

Accurate prostate segmentation in TRUS imagery is an important step in different clinical applications, and it is particularly necessary for providing a 3-dimensional spatial prior to the image reconstruction of trans-rectal optical tomography for prostate cancer detection. 2-dimensional segmentation of the TRUS images is challenging, due to more complexities in contrast, morphological features and image artifacts, as well as significant inter-subject variations of the prostate shape and size.

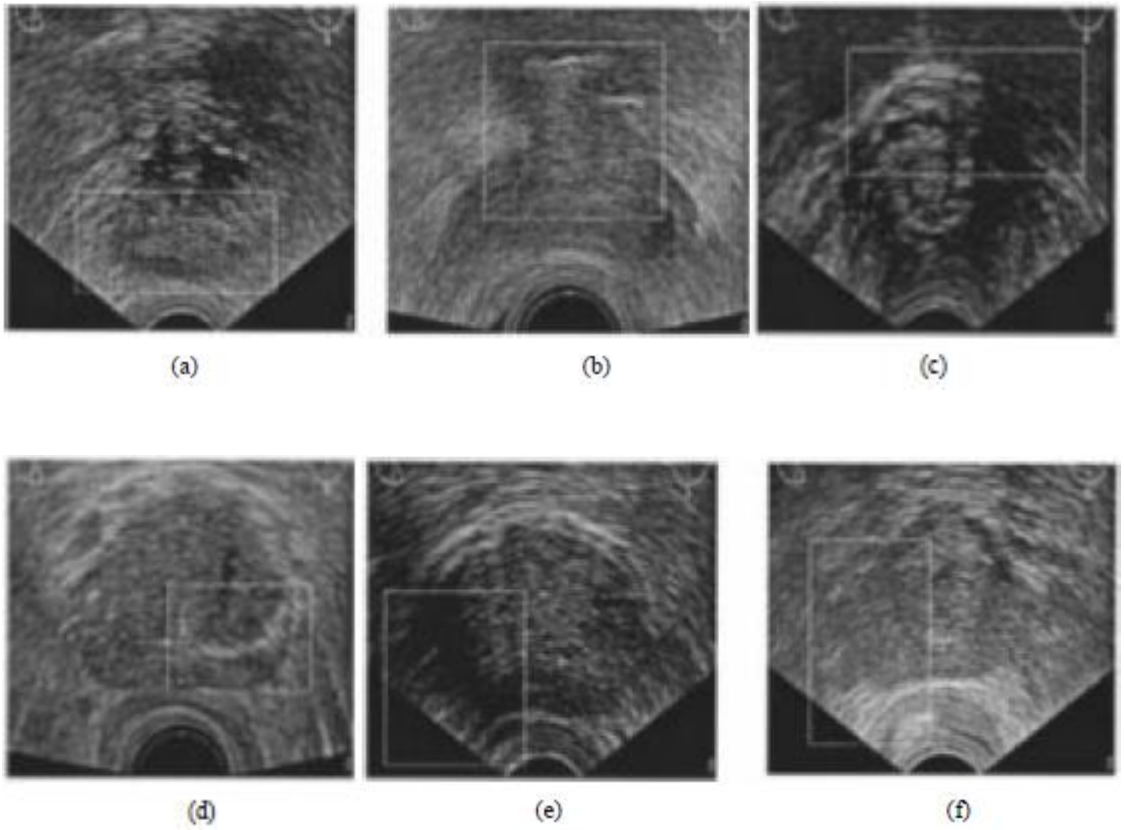

Figure 2.13 Examples of different prostate images with artifacts that make automatic segmentation of the gland difficult. The rectangle in each image indicates the artifact described. Indistinct boundaries between the prostate and (a) seminal vesicles and (b) bladder neck near the base. (c) Echo from pubic arch near the apex. (d) Hyperechoic structure within the prostate due to corpora amylacea. (e) Occlusion of part of the prostate due to bowel gas. (f) Shadowing due to calcification in the anterior part of the prostate

Many algorithms have been proposed for prostate contouring. A statistical shape model is reported for automatic prostate segmentation [44].

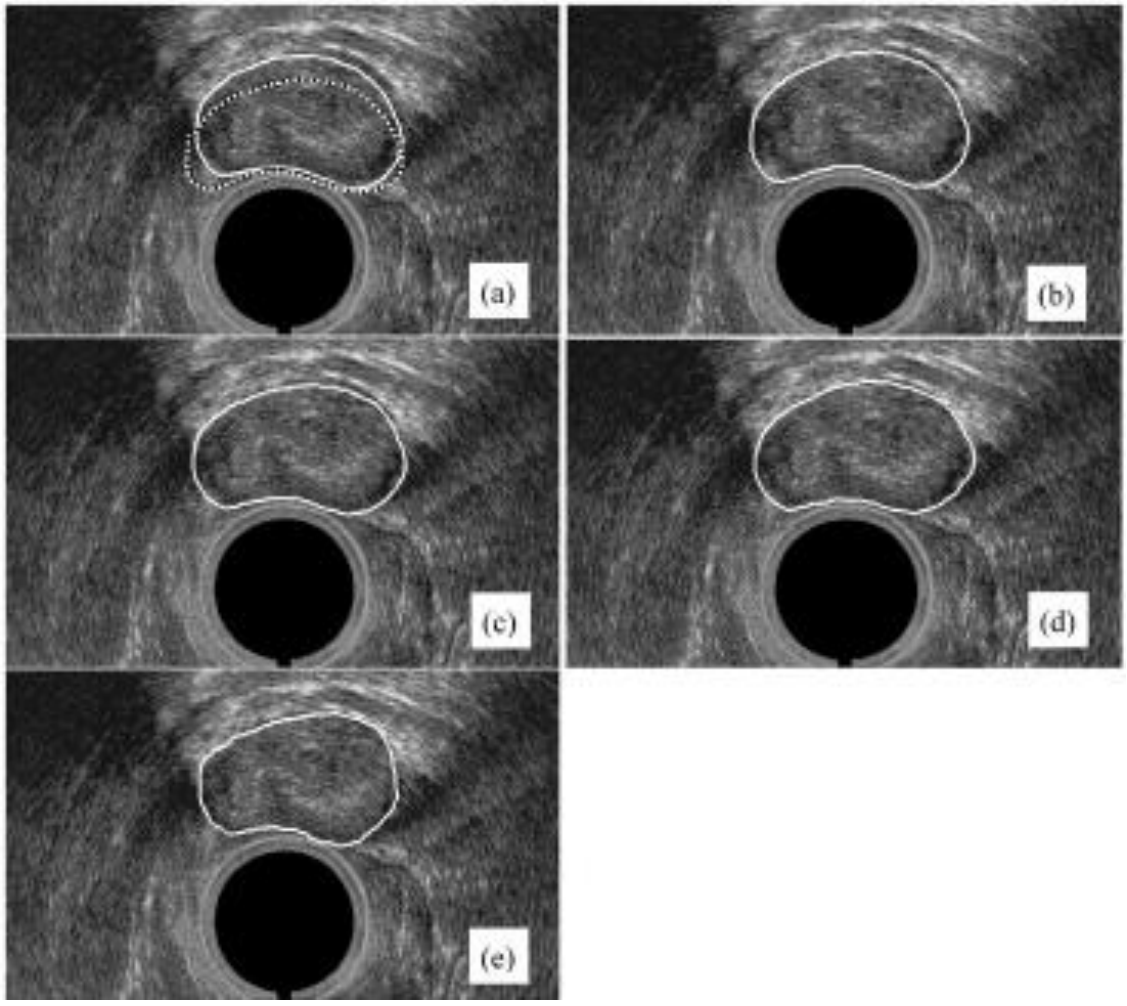

Figure 2.14 Demonstration of method proposed in [44] with MRI.

In this method, a Gabor filter bank is first used to characterize the prostate boundaries in ultrasound images in both multiple scales and multiple orientations. The Gabor features are further reconstructed to be invariant to the rotation of the ultrasound probe and incorporated in the prostate model as image attributes for guiding a deformable model that converges to prostate boundary in a coarse to fine approach. This method requires prior information about the size of the prostate in order to train the system. There are many prostate segmentation algorithms for ultrasound images. An algorithm proposed in a study [45] uses an anisotropic diffusion filter and patient specific anatomical information.

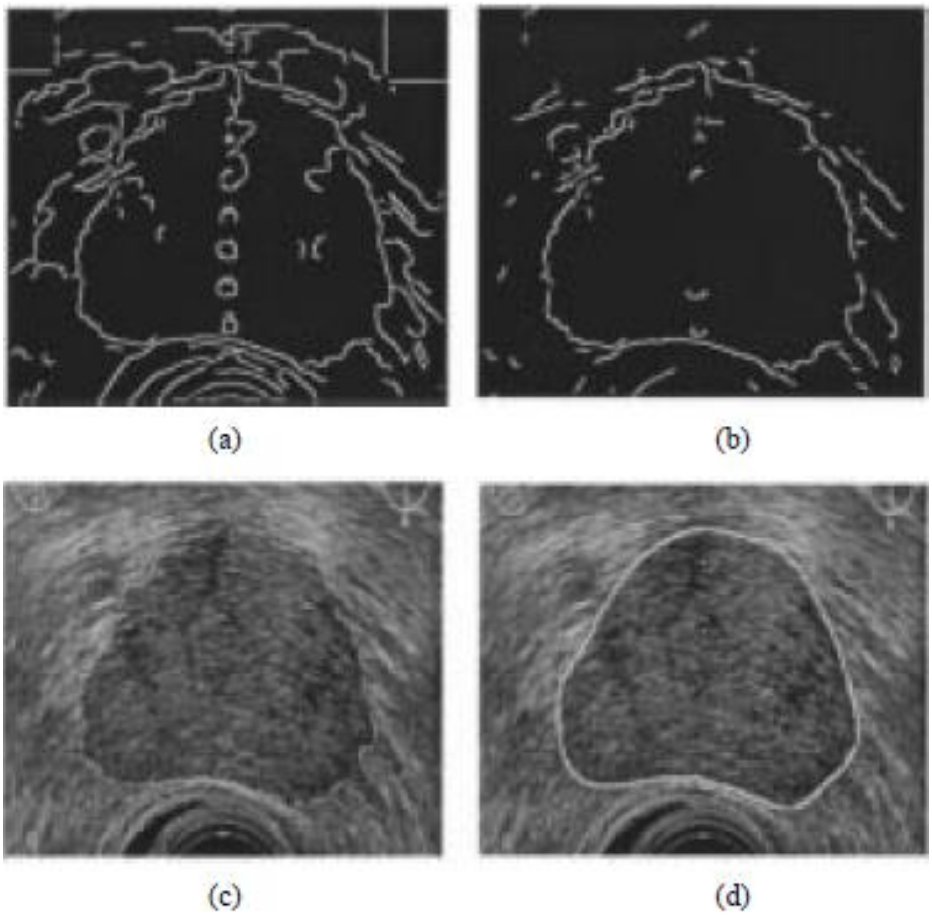

Figure 2.15 Detection of edges before and after weak membrane fitting in paper [45] with MRI. (a) Detected edges before a priori knowledge-based filtering. (b) Edge image after removal of false edges using knowledge-based filtering. (c) Edges overlaid on top of the prostate image. (d) Final boundary delineation on the prostate image.

In this paper, guided edge delineation is described, which involves presenting automatically detected prostate edges as a visual guide to the observer, followed by manual editing. It helps an expert radiologist to manually segment the images.

Quadratic wavelet spline and an active contour model that evolves across edge maps at different resolutions of a wavelet transform to converge to the prostate contour are proposed in a recent study [46].

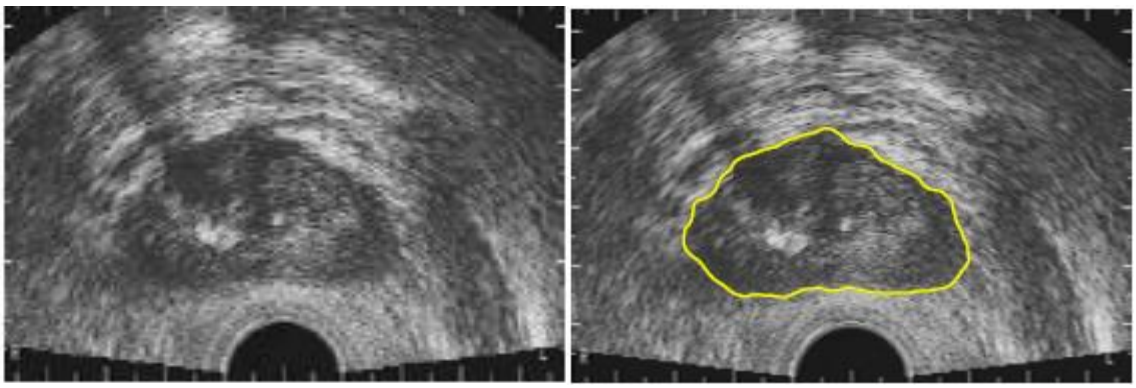

(a) (b)

Figure 2.16 (a) Original image and (b) segmented prostate profile from [46]

This paper presents a semi-automatic prostate contour extraction scheme, which is based on the wavelet transform and active contour models, or snakes. The ultrasound image is first decomposed into edge maps at different resolutions via the wavelet transform. Seed points are found in the coarsest edge map by examining the maxima along the radial profiles which emanate from an anchor point selected manually. These seed points are used to initialize a snake, which will evolve across the edge maps at different resolutions and eventually converge to the contour of the prostate.

A Study in [47] Proposes approach of AAM propagation from probabilistic texture information estimated in a Bayesian framework with prior shape and posterior probability with the goal of segmenting the prostate in 2D TRUS images.

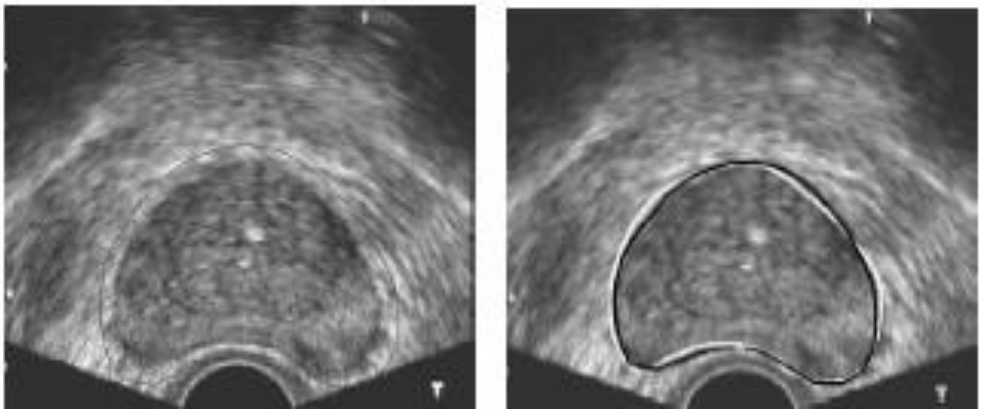

(a) (b)

Figure 2.17 (a) Automatic initialization of the mean model and (b) Final segmentation result from [47]

In paper [48], authors have developed a radial bas-relief (RBR) method, which is adopted and extended from a darkroom technique used in conventional photography (i.e. bas-relief), to segment the prostate boundary from TRUS. The proposed method consists of 3 steps: (1) image inversion, (2) image panning (to provide a position offset register by moving every pixel radically from the center of the image by a certain distance), and (3) dual-image addition (superimposing positive and negative images). The smoothed, binary image is then inverted again to switch the boundary areas to the foreground

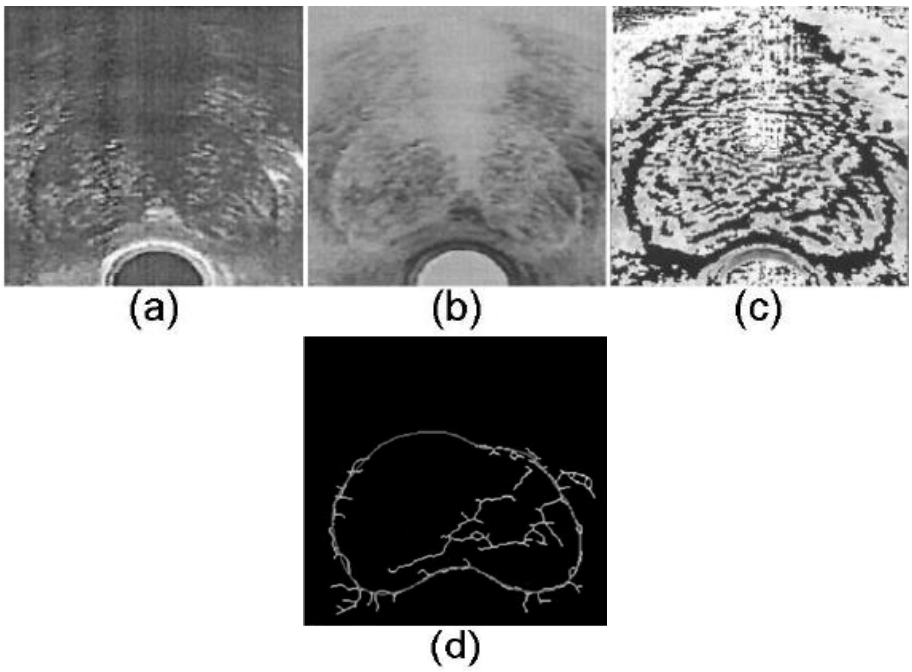

Figure 2.18 (a)original image, (b)inverted image, (c) RBR processed image (d) final segmented image

To efficiently detect the prostate boundary, in [49], they developed a method based on a deformable contour model, named the discrete dynamic contour (DDC). In this method, initialization requires the user to select only 4 points (Fig. 2.18 a) from which the outline of the prostate is estimated by cubic interpolation functions and shape information. To improve the model's performance, gradient direction information is used during deformation to push the model toward the boundaries. However, the success of their approach is dependent on the careful initialization of the contour (Fig. 2.18 b), which requires the user to select points on the prostate boundary. To overcome this drawback, the authors added a tool to edit the detected boundary and then re-deform it (Fig. 2.18, c and d).

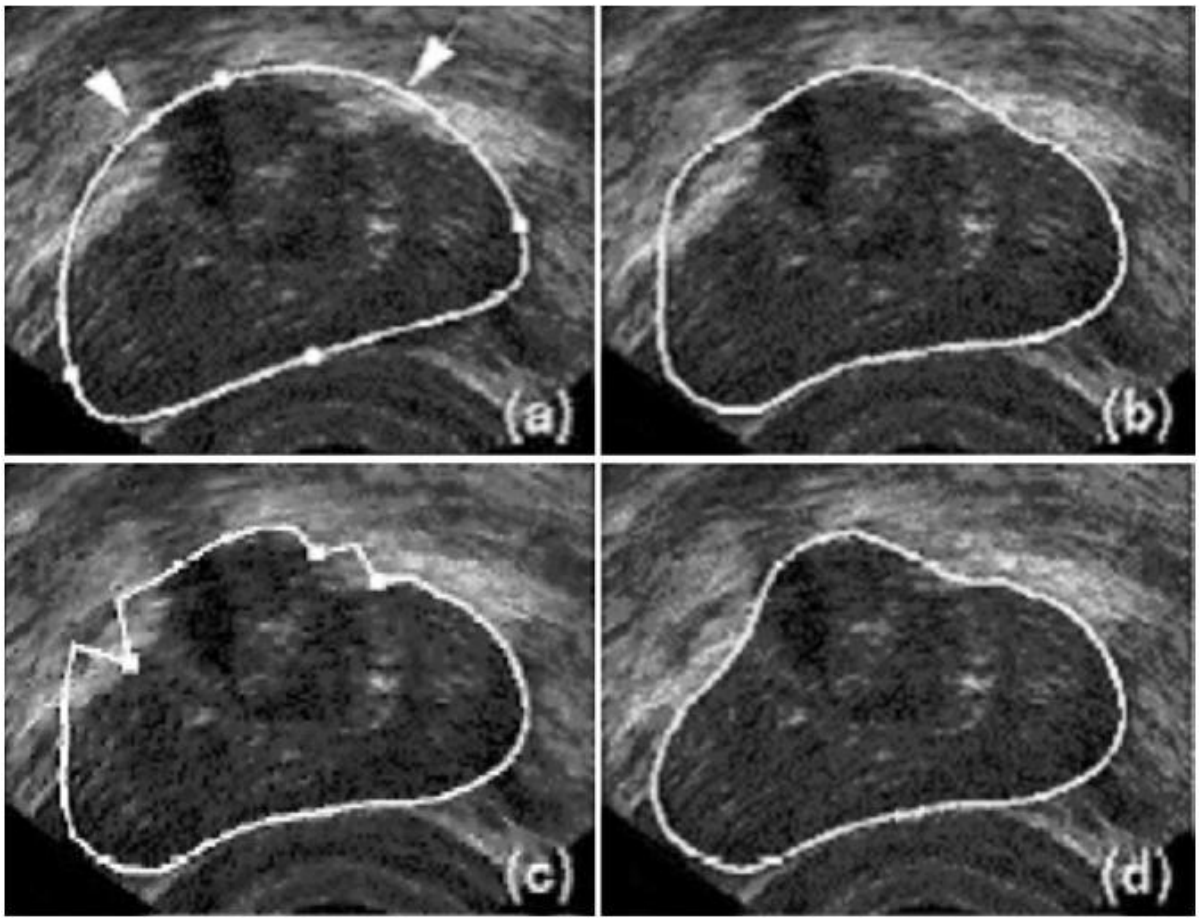

Figure 2.19 Prostate boundary detection by DDC. (a) Initial DDC, (b) after initial deformation, (c) 3 points (indicated by squares) were edited and clamped; d, after second deformation.

Other proposed approaches use Gabor filter texture segmentation [49] and morphological operators [50]. Most of the developed techniques use deformable model concepts in segmenting prostate images.

We use Snakes active control model [50] along with manual contouring for prostate segmentation from a TRUS image. A snake is an energy-minimizing spline guided by external constraint forces and influenced by image forces that pull it toward features such as lines and edges. Snakes are active contour models: they lock onto nearby edges, localizing them accurately. Scale-space continuation can be used to enlarge the capture region surrounding a feature. Snakes

provide a unified account of a number of visual problems, including detection of edges, lines, and subjective contours, motion tracking, and stereo matching.

2.5 Optical Properties of Canine and Human Prostate

Dogs have been previously used for prostate tumor model studies because of the morphological and functional similarities between canine and human prostate glands. Interpretation of the "noninvasively" acquired optical tomography images of the prostate relies on previous knowledge of prostate optical properties; therefore, a summary of what is known regarding the optical properties of both the canine and human prostate is also necessary. For the prostate, there is limited information regarding optical characteristic of prostatic tissue as well as oxygenation of intact prostatic tissue [51]. Using light to image prostate cancer will not be achievable unless benign and cancerous prostate tissues present different optical properties that can be resolved by means of optical interrogation. Revealing the contrast of prostate cancer over normal tissue is challenging. There are many studies on prostate optical properties using different wavelengths and methods [52]. The prostate of a dog is usually considered as a model closest to that of a human being. Therefore, numbers of studies have been conducted on canine subjects to estimate optical properties of the prostate.

CHAPTER 3

3-D PROFILING OF CANINE PROSTATE FOR IMAGE RECONSTRUCTION

The approach we follow starts with 2-D image segmentation of TRUS images using a Snake algorithm. Then we find out the approximate position of axial planes followed by placement of these segmented contours in a 3-D space. The next step is to interpolate data points to obtain nodes and elements which are used for mesh generation of a prostate. We incorporate the prostate blob inside a rectangular mesh. The prostate blob is denser than the surrounding rectangular mesh acting as tissue, and it also has different optical properties than the surrounding rectangular mesh. The entire mesh volume is used as a spatial prior for DOT. It should be noted that the NIR data acquisition was not gated by the anesthesia instrument, so the 4-seconds NIR data acquisition could have had interference from the breathing of the dog, as well as possible movements or shifts of the hand-held trans-rectal probe during each cycle of NIR data acquisition.

3.1 Image Segmentation

In this study research we develop a routine of segmenting TRUS images obtained from canine prostate, based on the combination of a Snakes algorithm and selected manual segmentation.

3.1.1 Snake Algorithm [50]

It is a feature extraction based on energy minimization. Snake works with image forces that push the snake towards salient features like lines, edges and contours.

We can represent energy function as

$$E^{*}_{Snake} = \int_0^1 E_{Snake}\, v(s)ds = \int_0^1 [\, E_{int} v(s) + E_{image} v(s) + E_{con} v(s)\,]\, ds$$

$v(s) = (x(s), y(s))$, represents parametric position of snake

E_{int}, is spline due to bending,E_{image}, gives rise to the image forces, and E_{con}, gives rise to the external constraint forces.

Internal Energy

Internal spline energy can be represented as

$$E_{int} = (\alpha(s)|v_s|^2 + \beta(s)|v_{ss}|^2)/2$$

The spline energy is composed of a first order term controlled by $\alpha(s)$ and a second-order term controlled by $\beta(s)$. The first-order term makes the snake act like a membrane and the second-order term makes it act like a thin plate. Adjusting the weights $\alpha(s)$ and $\beta(s)$ controls the relative importance of the membrane and thin-plate terms. Setting $\beta(s)$ to zero at a point allows the snake to become second-order discontinuous and develop a corner. The controlled continuity spline is a generalization of a Tikonov stabilizer.

- **Image Energy**

The total image energy can be expressed as a weighted combination of the three energy functionals as

$$E_{image} = w_{line} E_{line} + w_{edge} E_{edge} + w_{term} E_{term}$$

Line functional is the image intensity represented as

$$E_{line} = I(x, y)$$

Snake will be attracted either to dark lines of light lines depending on the sign of w_{line}. Depending on other constraints snake aligns itself with the lightest or the darkest contour.

Edge functional can be calculated by simply taking the image gradient as

$$E_{edge} = -|\nabla I(x, y)|^2$$

Snake is attracted to contours with large image gradients.

If part of a snake finds a low energy image feature, the spline term will pull neighboring parts of the snake toward a possible continuation of the feature. This effectively places a large energy well around a good local minimum. A similar effect can be achieved by spatially smoothing the edge or line-energy functional. One can allow the snake to come to equilibrium.

To find terminations of lines and corners, the curvature of level lines in a slightly smoothed image is used as

$$C(x, y) = G_\sigma(x, y) * I(x, y)$$

$\theta = \tan^{-1}\left(\frac{C_y}{C_x}\right)$ is the gradient angle. $n = (\cos\theta, \sin\theta)$ is a unit vector along the gradient direction and $\hat{n} = (-\sin\theta, \cos\theta)$ is unit vector perpendicular to gradient direction. Then curvature of level contours in $C(x, y)$ can be written as

$$E_{term} = \frac{\partial\theta}{\partial\hat{n}}$$

$$= \frac{\partial^2 C/\partial n^2}{\partial C/\partial n}$$

$$= \frac{C_{yy}C_x^2 - 2C_{xy}C_xC_y + C_{xx}C_y^2}{(C_x^2 + C_y^2)^{\frac{3}{2}}}$$

Combining E_{term} and E_{edge}gives a snake that is attracted to edges or terminations.

External Energy

$$E_{ext} = E_{image} + E_{con}$$

When $\alpha(s) = \alpha$ and $\beta(s) = \beta$ are constants, minimizing energy function

$$E^*_{Snake} = \int_0^1 [\, E_{int}v(s) + E_{image}v(s) + E_{con}v(s) \,]\, ds$$

gives rise to two independent Euler equations

$$\alpha x_{ss} + \beta x_{ssss} + \frac{\partial E_{ext}}{\partial x} = 0$$

$$\alpha y_{ss} + \beta y_{ssss} + \frac{\partial E_{ext}}{\partial y} = 0$$

When $\alpha(s)$ and $\beta(s)$ are not constant,

$$E^*_{Snake} = \sum_{i=1}^{n} E_{int}(i) + E_{ext}(i)$$

$$E_{int}(i) = \frac{\alpha_i |v_i - v_{i-1}|^2}{2h^2} + \frac{\beta_i |v_{i-1} - 2v_i + v_{i+1}|^2}{2h^4}$$

Where, v(0) = v(n).

Corresponding Euler equations are

$$\alpha_i(v_i - v_{i-1}) - \alpha_{i+1}(v_{i+1} - v_i) + \beta_{i-1}(v_{i-2} - 2v_{i-1} + v_i) - 2\beta_i(v_{i-1} - 2v_i + v_{i+1})$$
$$+ \beta_{i+1}(v_i - 2v_{i+1} + v_{i+2}) + (f_x(i), f_y(i)) = 0$$

Where,

$$f_x(i) = \frac{\partial E_{ext}}{\partial x_i}$$

and

$$f_y(i) = \frac{\partial E_{ext}}{\partial y_i}$$

The method is implicit with respect to the internal forces, so it can solve very rigid snakes with large step sizes. If the external forces become large, the explicit Euler steps of the external forces will require much smaller step sizes.

The basic snake behavior algorithm:

1) Decide region of interest from an image and initial points are defined around feature to be segmented.

2) Move all these points through an iterative process where energy function for each point is minimized.

3) Calculate energy function for each point in the local neighbourhood.

4) Move the snake to point with lowest energy function.

5) Repeat for every point.

6) Iterate until termination conditions like number of iterations or stability criteria are met.

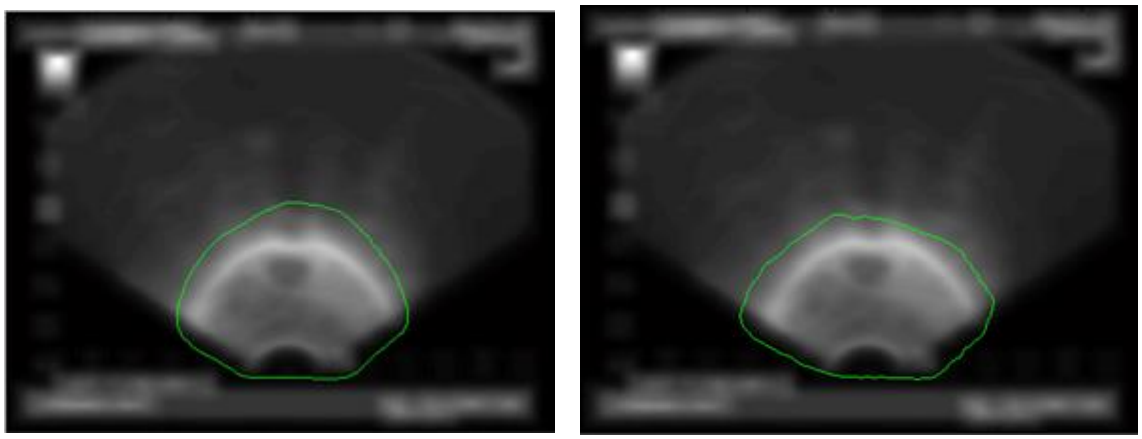

Figure 3.1 TRUS image segmentation using Snake

Total Energy = α. Continuity + β. Curvature + γ. Image. If α is higher, more important is the distance between points is minimized. Higher the β, the more important that angles are maximized. The higher γ, the more important the edges are. If β is set to 0, snake finds the corners from an image.

3.1.2 Manual Contour Tracking

2-dimensional segmentation of the axial TRUS images are performed extensively, however, 2-dimensional segmentation of the sagittal TRUS images are challenging, due to more complexities in contrast, morphological features and image artifacts, as well as significant inter-subject variations of the prostate shape and size. For such cases we draw a contour manually by hand to get accurate contour of 2-dimensional axial as well as sagittal images.

An interactive program takes the input from an expert in the field and manually segmented contours are obtained for 3D profiling of a prostate. We segment 3 axial images of prostate, one on cranial side, one in middle and one on caudal side of prostate. Sagittal image in the middle section is segmented as a reference for 3-D contour profiling.

(a) (b) (c)

Figure 3.2 Manual contour tracking for (a) cranial side of prostate (b) mid part of prostate (c) caudal side of prostate

3.2 Approximation of Position of 2-D Segmented Prostate Contours

It is important to find the position of sparsely acquired 2-D axial images in order to profile more accurate 3-D model of a prostate. We have a set of axial images taken at different positions. We use a sagittal profile of a prostate to find out the approximate location of an axial plane segmented from 2-D TRUS axial images.

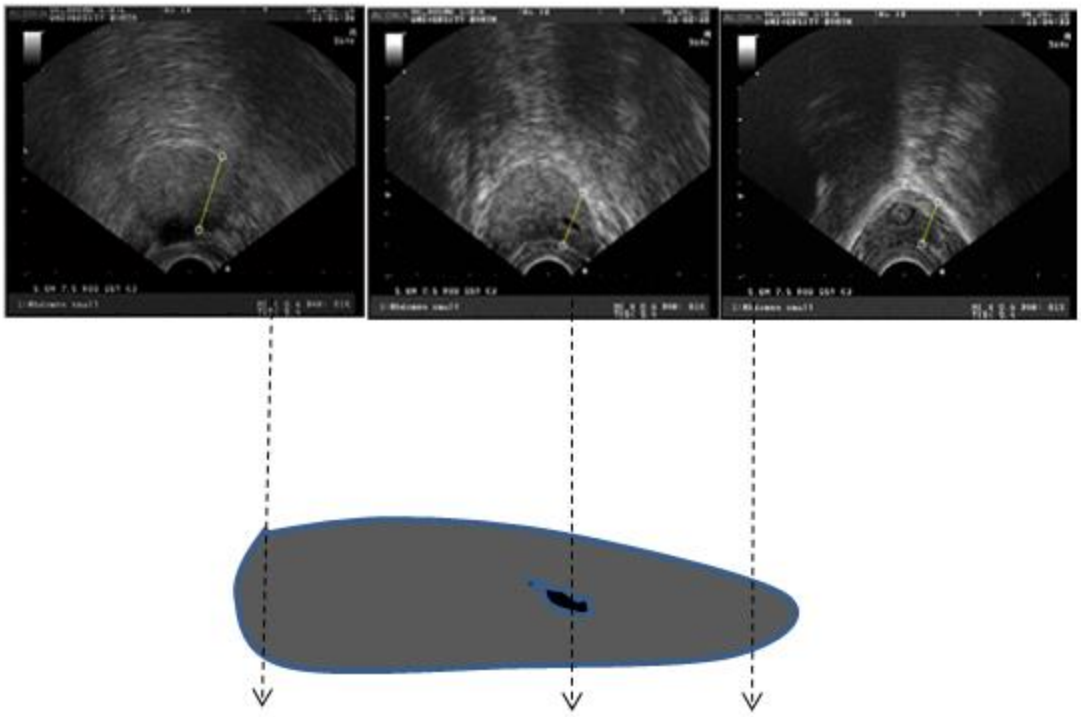

Figure 3.3 Position approximation of axial planes based on 2-d sagittal image as reference

3.3 3-D Profiling of Canine Prostate

Earlier step gives idea about where the axial planes are approximately positioned in 3D space of prostate profile. We align the segmented axial contours according to the axial positions and use interpolation to construct new data points using the points on axial segmented contour to obtain a complete 3D profile of a prostate.

3.3.1 Interpolation

Different types of interpolation techniques include linear, polynomial, Gaussian interpolation. As we want a smooth profile, we use spline interpolation along a curve using the points on axial contours. Depending on the density of points required we can construct new data points in

between. We use segmented sagittal contour to compare with the interpolated 3-D profile of a prostate.

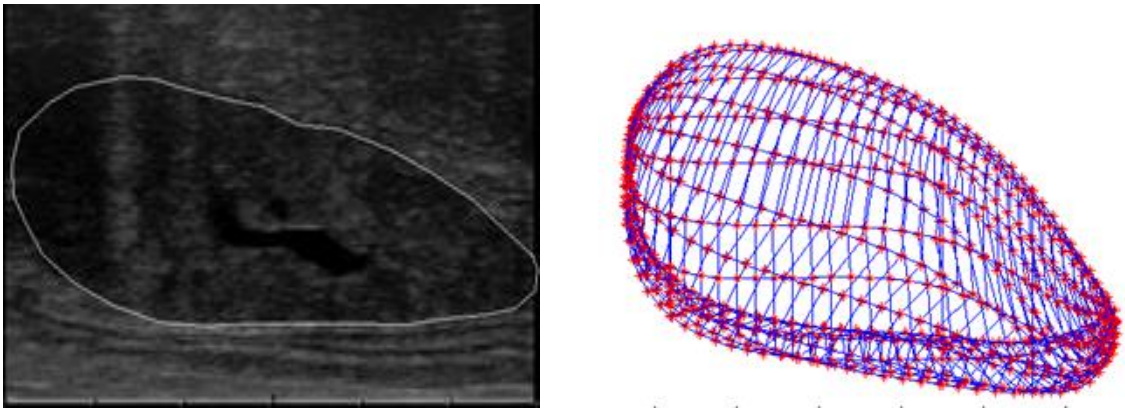

(a) (b)

Figure 3.4 (a) Sagittal image of prostate used as a reference for (b) interpolated prostate profile

The 3-D profile of a prostate is quite close to the actual sagittal view of prostate. It looks a little tilted due to limited information from images obtained using TRUS imaging.

3.3.2 Mesh Generation

Next step is to create a 3-D mesh from obtained 3-D prostate profile. Meshes are categorized according to their dimensionality and choice of elements. Triangular meshes, tetrahedral meshes, quadrilateral meshes, and hexahedral meshes are named according to the shapes of their elements. Tetrahedral elements are the simplest of all polyhedral shapes, having four vertices and four triangular faces.

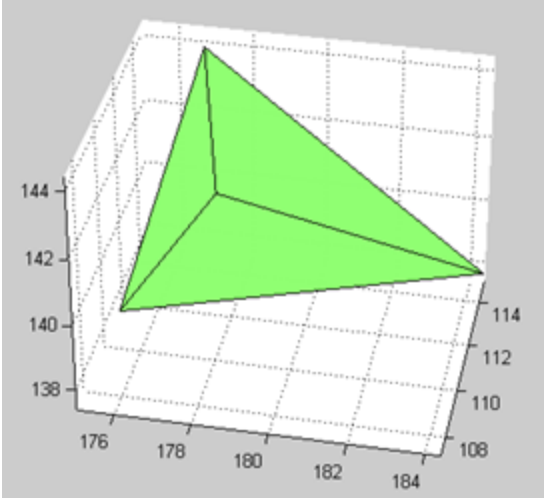

Figure 3.5 Basic block of a mesh-tetrahedron using Delaunay triangulation

Meshes are also classified as structured and unstructured meshes. Structured meshes are suitable primarily for domains that have tractable geometries and do not require a strongly graded mesh. Unstructured meshes are much more versatile because of their ability to combine good element shapes with odd domain shapes and element sizes that grade from very small to very large. For most applications, the elements constituting a mesh must intersect nicely meaning that if two elements intersect, their intersection is a vertex or edge or entire face of both [28].

3.3.2.1 Delaunay triangulation

Delaunay triangulations are widely used in scientific computing in many diverse applications. While there are numerous algorithms for computing triangulations, it is the favorable geometric properties of the Delaunay triangulation that make it so useful.

The fundamental property is the Delaunay criterion. In the case of 2-D triangulations, this is often called the empty circumcircle criterion. For a set of points in 2-D, a Delaunay triangulation of these points ensures the circumcircle associated with each triangle contains no

other point in its interior. This property is important. In the illustration below, the circumcircle associated with T1 is empty. It does not contain a point in its interior. The circumcircle associated with T2 is empty. It does not contain a point in its interior. This triangulation is a Delaunay triangulation.

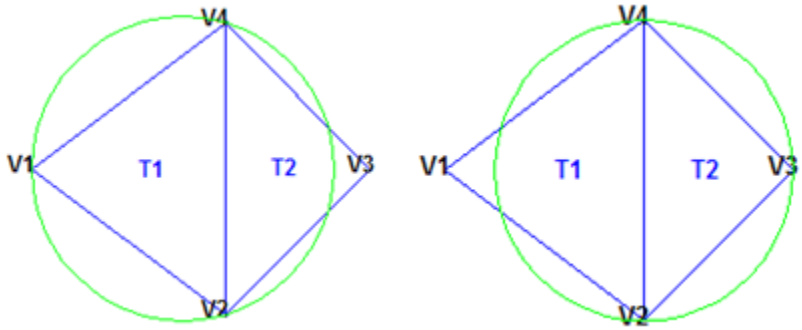

Figure 3.6 Illustration-1 for Delaunay triangulation

The triangles below are different. The circumcircle associated with T1 is not empty. It contains V3 in its interior. The circumcircle associated with T2 is not empty. It contains V1 in its interior. This triangulation is *not* a Delaunay triangulation.

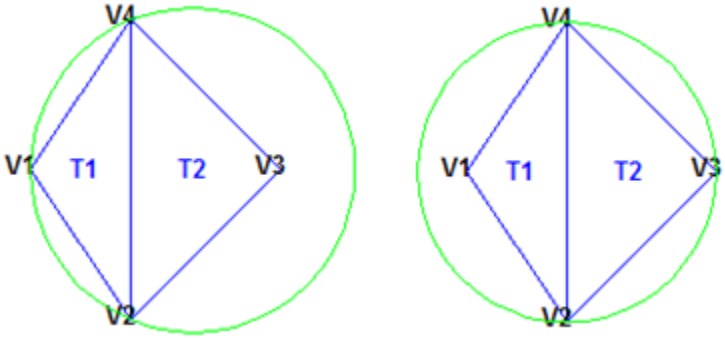

Figure 3.7 Illustration-2 for Delaunay triangulation

Delaunay triangles are said to be "well shaped" because in fulfilling the empty circumcircle property, triangles with large internal angles are selected over ones with small internal angles. The triangles in the non-Delaunay triangulation have sharp angles at vertices V2 and V4. If the edge {V2, V4} were replaced by an edge joining V1 and V3, the minimum angle would be maximized and the triangulation would become a Delaunay triangulation. Also, the Delaunay triangulation connects points in a nearest-neighbor manner. These two characteristics, well-shaped triangles and the nearest-neighbor relation have important implications in practice and motivate the use of Delaunay triangulations in scattered data interpolation.

While the Delaunay property is well defined, the topology of the triangulation is not unique in the presence of degenerate point sets. In two dimensions, degeneracies arise when four or more unique points lie on the same circle. The vertices of a square, for example, have a non-unique Delaunay triangulation.

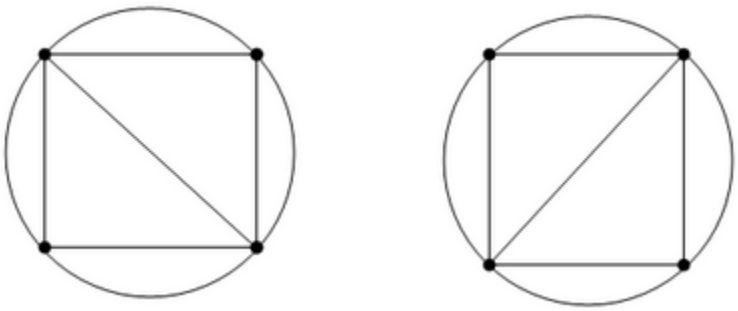

Figure 3.8 Non-unique Delaunay triangulation

The properties of Delaunay triangulations extend to higher dimensions. The triangulation of a 3-D set of points is composed of tetrahedra. The next illustration shows a simple 3-D

Delaunay triangulation made up of two tetrahedra. The circumsphere of one tetrahedron is shown to highlight the empty circumsphere criterion.

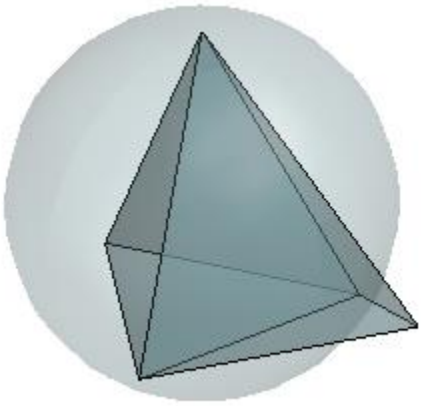

Figure 3.9 Delaunay triangulation for 3-D

3.3.2.2 Prostate Blob with Outer Rectangular Mesh

Rectangular mesh which is used as equivalent to tissue around prostate based on bi-planar TRUS transducer shown in fig. 3.10 (a). A working geometry of the NIR array for coupling to TRUS has 7 channels on each lateral side of the TRUS to span 60mm longitudinally as the TRUS transducer window does and the optical channels have 10mm spacing. The NIR array leaves the 10 mm-wide sagittal TRUS transducer unblocked; therefore there is 20mm separation of the NIR optodes from one lateral side to the other. These considerations lead to the NIR array geometry generated by a group member previously is shown in fig. 3.10 (c) where 14 optodes are spaced 10mm longitudinally and 20mm laterally. fig. 3.10 (d) illustrates an NIR/US probe if the sagittal NIR array can be fabricated synergistically with the TRUS probe.

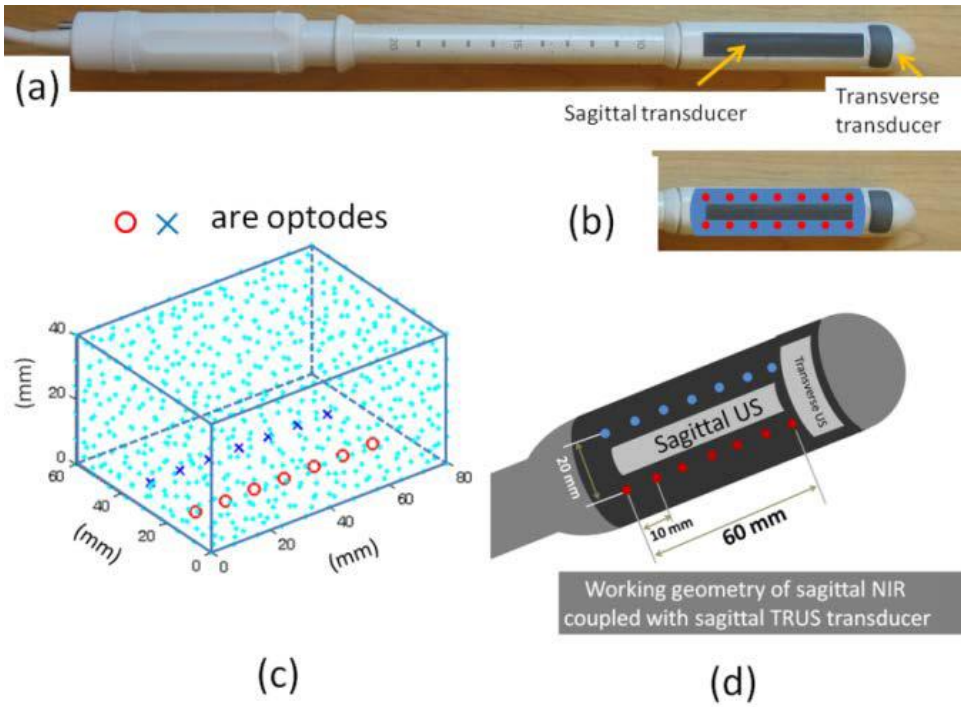

Figure 3.10 Geometry of the TRUS-DOT combined probe (a) Photograph of a bi-plane TRUS transducer. (b) A feasible geometry of NIR array for coupling with sagittal TRUS transducer. (c) The NIR imaging geometry for the one depicted in (b). (d) Cartoon-art illustration of a fully-integrated sagittal trans-rectal NIR/US probe.

We use Delaunay triangulation to form a 3-D tetrahedral mesh of prostate profile which can be used as spatial prior for optical tomography reconstruction. Surface nodes and internal nodes of the 3-D profile are used as tetrahedral vertices to give input to Delaunay triangulation. Tetrahedral mesh formation using Delaunay triangulation is shown in fig. 3.11.

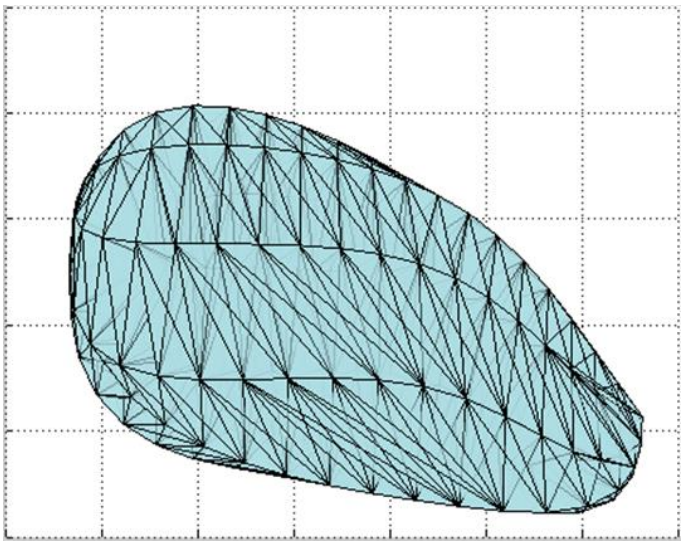

Figure 3.11 3-D profile of prostate using Delaunay triangulation

The parallel-linear geometry of the optical source-array and detector-array entails 3-dimensional optical tomography reconstruction; however, due to the 2-dimensional ultrasonography only the middle sagittal image of optical tomography has an ultrasound image to correlate with. The optical tomography reconstruction was performed in a volume of 80 mm X 70 mm X 50 mm (cranial-to-caudal X right-lateral-to-left-lateral X dorsal-to-ventral), and a 60 mm X 40 mm view of middle sagittal image of optical tomography was extracted to correlate with the middle sagittal ultrasound image of the same dimension, as detailed in Fig. 3.12(a). Hence, we want to form a rectangular mesh enclosing the prostate blob mesh.

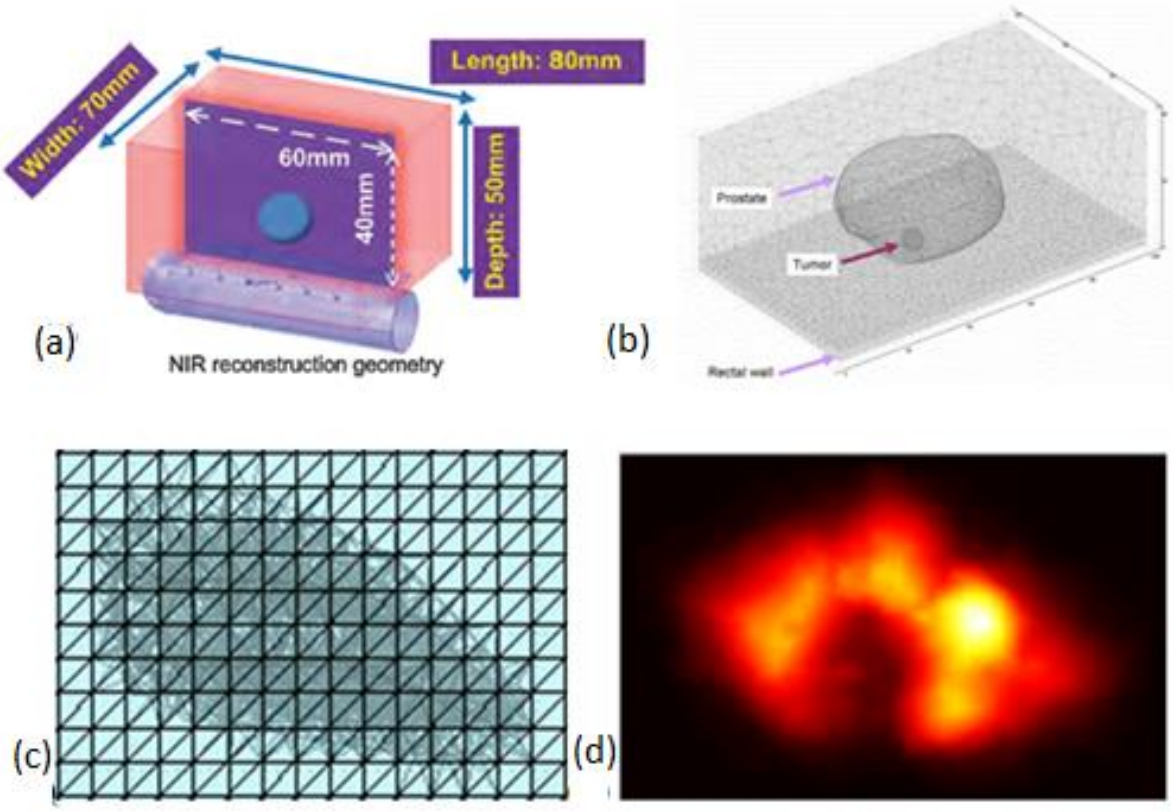

Figure 3.12 (a) NIR reconstruction geometry, (b) Mesh illustrating outer tissue, prostate and tumor, (c) Prostate blob inside rectangular mesh (d) NIR image reconstruction showing prostate profile inside tissue.

Fig. 3.12 (b) gives an illustration of how prostate blob and a rectangular mesh can be arranged before giving an input to NIRFAST. Fig. 3.12 (c) shows prostate blob embedded inside a rectangular mesh. This mesh is now used as spatial prior for optical tomography reconstruction using NIRFAST. Fig. 3.12 (d) shows the optical tomography reconstruction using TRUS image and prostate profile mesh.

CHAPTER 4

NIR Optical Tomography using NIRFAST

Diffuse optical tomography (DOT), also known as near infrared tomography, has been under investigation, for non-invasive functional imaging of tissue, specifically for the detection and characterization of breast cancer or other soft tissue lesions. Much work has been carried out for accurate modeling and image reconstruction from clinical data. NIRFAST (Near-infrared Frequency domain absorption and Scatter Tomography) is a modeling and image reconstruction package, which is capable of single wavelength and multi-wavelength optical or functional imaging from measured data. NIRFAST is for general frequency-domain DOT, i.e., the light intensity is modulated.

Theory [53]

Near Infrared Frequency Domain Absorption and Scatter Tomography is an FEM based package designed for modeling Near-Infrared light transport in tissue. This includes standard single wavelength absorption and reduced scatter, multi-wavelength spectrally constrained models, fluorescence models

4.1 The Forward Model

The technique of determining what a given sensor would measure in a given formation and environment by applying a set of theoretical equations for the sensor response is called the forward modeling. If the magnitude of the isotropic fluence within tissue is significantly larger

than the directional flux magnitude, the light field is 'diffuse', which occurs when the scattering interactions dominate over absorption and the region of interest is far from sources and boundaries provided the light fluence is not rapidly changing with time (i.e. such as in the sub-picosecond time frame).

The diffusion approximation in the frequency domain is given by

$$-\nabla.\kappa(r)\nabla\phi(\mathrm{r},\omega)+\left(\mu_a+\frac{i\omega}{c_m(r)}\right)\phi(\mathrm{r},\omega)=q_0(\mathrm{r},\omega)$$

where μ_a and μ'_s are absorption and reduced scattering coefficients, respectively, $q_0(\mathrm{r},\omega)$ is an isotropic source term, $\phi(\mathrm{r},\omega)$ is the photon fluence rate at position r, and modulation frequency,ω, $\kappa=1/3(\mu_a+\mu'_s)$ is the diffusion coefficient and $c_m(r)$ is the speed of light in the medium at any point, defined by $c_m/n(r)$, where $n(r)$ is the index of refraction at the same point and c_m is the speed of light in vacuum.

We use finite-element method to solve equation for $q_0(\mathrm{r},\omega)$ under the Robin-type boundary condition [54]

$$\phi(\mathrm{r}_0,\omega)+2\kappa A\widehat{n_0}.\nabla\phi(\mathrm{r}_0,\omega)=0$$

at the boundary , r_0 where $\widehat{n_0}$ is the outward normal vector of the boundary, *A* is the refractive index mismatch coefficient. The refractive indices of air and tissue are 1 and 1.33 respectively, for the tissue-air boundary, leading to *A*=2.82 as in [54].

The flux leaving the external boundary is equal to the fluence rate at the boundary weighted by a factor that accounts for the internal reflection of light back into the tissue. This relationship is described in the following equation

$$\phi(\xi,\omega)+2A\hat{n}.\kappa(\xi)\nabla\phi(\xi,\omega)=0$$

where ξ is a point on the external boundary, $\hat{n}$ is the outward pointing normal, and A depends upon the relative refractive index (RI) mismatch between the tissue domain Ω and air. Here, A can be derived from Fresnel's law

$$A = \frac{\frac{2}{(1-R_0)} - 1 + |\cos\theta_c|^3}{1 - |\cos\theta_c|^2}$$

where $V_c = \arcsin(\frac{n_{AIR}}{n_1})$, the angle at which total internal reflection occurs for photons moving from region Ω with RI n_1 to air with RI n_{AIR}, and $R_0 = (\frac{n_1}{n_{AIR}} - 1)^2/(\frac{n_1}{n_{AIR}} + 1)^2$, At the external boundaries, RI is generally assumed to be equal to that of free space, so that n_{AIR}=1.

When the RI is homogeneous, the finite element discretization of a volume, Ω, can be obtained by subdividing the domain into D elements joined at V vertex nodes. The diffusion equation in the FEM framework can be expressed as a system of linear algebraic equations

$$\left(K(\kappa) + C\left(\mu_a + \frac{i\omega}{c_m}\right) + \frac{1}{(2A)}F\right)\phi = q_0$$

$C\left(\mu_a + \frac{i\omega}{c_m}\right)$ and F have entries given by

$$K_{ij} = \int \kappa(r)\nabla u_i(r).\nabla u_j(r)d^n r$$

$$C_{ij} = \int \left(\mu_a(r) + \frac{i\omega}{c_m(r)}\right)u_i(r)u_j(r)d^n r$$

$$F_{ij} = \oint u_i(r)u_j(r)d^{n-1}r$$

And source vector q_0 has terms

$$q_{0i} = \int u_i(r) q_0(r) d^n r$$

The source term is defined as a distributed, Gaussian source, matching the intensity profile at the tip of the optical fiber.

4.2 The inverse Model

The inverse problem consists in using the results of actual observations to infer the values of the parameters characterizing the system under investigation. The goal of the inverse problem is the recovery of optical properties $\mu = (\mu_a, \kappa)$ at each FEM node within the domain using measurements of light fluence from the tissue surface. This inversion can be achieved using a modified-Tikhonov minimization. If the measured fluence at the tissue surface is represented by ϕ^M and the calculated data using the forward solver by ϕ^C, then the standard Tikhonov minimization function is given by

$$\chi^2 = \min_{\mu} \left\{ \sum_{i=1}^{NM} \left(\phi_i^M - \phi_i^C\right)^2 + \lambda \sum_{j=1}^{NN} \left(\mu_j - \mu_0\right)^2 \right\}$$

where NM is the total number of measurements obtained from the imaging device, NN is the number of FEM nodes (the unknowns). λ is the Tikhonov regularization parameter, which is defined as the ratio of the variances of the measurement data and optical properties. μ_0 is either the initial estimate of the optical properties, generally obtained by data-calibration procedure, or it can be an *a priori* optical property distribution, which may be available. The minimization with respect to μ in Equation

$$\left(\frac{\partial \phi^C}{\partial \mu}\right)^T (\phi^M - \phi^C) - \lambda(\mu - \mu_0) = 0$$

The derivative matrix $\left(\frac{\partial \phi^C}{\partial \mu}\right)$ is known as the Jacobian matrix, *J*, and is also referred to as the weight or sensitivity matrix. Using this linear approximation of the problem, and solving it as an iterative scheme gives

$$(J^T J + \lambda I)\delta\mu = J^T \delta\phi - \lambda(\mu_i - \mu_0)$$

where $\delta\mu$ is the update for the optical properties and $\delta\phi$ is the data-model misfit at the current iteration. *I* is the identity matrix. A slight modification of above equation is known as the Levenberg–Marquardt (LM) procedure, where $\delta\mu = (\mu_i - \mu_0)$ is assumed in which case

$$\left(J^T J + \bar{\lambda} I\right)^{-1} J^T \delta\phi = \delta\mu$$

Where $\bar{\lambda} \equiv 2\lambda$. Also note that in LM procedure, the $\bar{\lambda}$ is monotonically decreased over the iterations [55]. The Jacobian defines the relationship between changes in boundary data ϕ^C, resulting from small changes in optical properties $\delta\mu = (\mu_i - \mu_0)$. Since both amplitude and phase data types are available from a frequency domain system, and since the problem considers the effects of absorption and diffusion, the structure of the Jacobian becomes

$$J = \begin{bmatrix} \frac{\delta lnI_1}{\delta\kappa_1} & \frac{\delta lnI_1}{\delta\kappa_2} & \cdots & \frac{\delta lnI_1}{\delta\kappa_{NN}}; & \frac{\delta lnI_1}{\delta\mu_{a1}} & \frac{\delta lnI_1}{\delta\mu_{a2}} & \cdots & \frac{\delta lnI_1}{\delta\mu_{aNN}} \\ \frac{\delta\theta_1}{\delta\kappa_1} & \frac{\delta\theta_1}{\delta\kappa_2} & \cdots & \frac{\delta\theta_1}{\delta\kappa_{NN}}; & \frac{\delta\theta_1}{\delta\mu_{a1}} & \frac{\delta\theta_1}{\delta\mu_{a2}} & \cdots & \frac{\delta\theta_1}{\delta\mu_{aNN}} \\ \frac{\delta lnI_2}{\delta\kappa_1} & \frac{\delta lnI_2}{\delta\kappa_2} & \cdots & \frac{\delta lnI_2}{\delta\kappa_{NN}}; & \frac{\delta lnI_2}{\delta\mu_{a1}} & \frac{\delta lnI_2}{\delta\mu_{a2}} & \cdots & \frac{\delta lnI_2}{\delta\mu_{aNN}} \\ \frac{\delta\theta_2}{\delta\kappa_1} & \frac{\delta\theta_2}{\delta\kappa_2} & \cdots & \frac{\delta\theta_2}{\delta\kappa_{NN}}; & \frac{\delta\theta_2}{\delta\mu_{a1}} & \frac{\delta\theta_2}{\delta\mu_{a2}} & \cdots & \frac{\delta\theta_2}{\delta\mu_{aNN}} \\ \vdots & \vdots & \ddots & \vdots & \vdots & \vdots & \ddots & \vdots \\ \frac{\delta lnI_{NM}}{\delta\kappa_1} & \frac{\delta lnI_{NM}}{\delta\kappa_2} & \cdots & \frac{\delta lnI_{NM}}{\delta\kappa_{NN}}; & \frac{\delta lnI_{NM}}{\delta\mu_{a1}} & \frac{\delta lnI_{NM}}{\delta\mu_{a2}} & \cdots & \frac{\delta lnI_{NM}}{\delta\mu_{aNN}} \\ \frac{\delta\theta_{NM}}{\delta\kappa_1} & \frac{\delta\theta_1}{\delta\kappa_2} & \cdots & \frac{\delta\theta_{NM}}{\delta\kappa_{NN}}; & \frac{\delta\theta_{NM}}{\delta\mu_{a1}} & \frac{\delta\theta_{NM}}{\delta\mu_{a2}} & \cdots & \frac{\delta\theta_{NM}}{\delta\mu_{aNN}} \end{bmatrix}$$

where $\frac{\delta lnI_i}{\delta \kappa_j}$ and $\frac{\delta lnI_i}{\delta \mu_{aj}}$ are the sub-matrices that define the change in log of amplitude of the i th measurement arising from a small change in κ and μ_a at the j th reconstructed node respectively; $\frac{\delta \theta_i}{\delta \kappa_j}$ and $\frac{\delta \theta_i}{\delta \mu_{aj}}$ are the sub-matrices that give the change in phase of the i th measurement arising from a change in κ and μ_a at the j th node, respectively. Jacobian in the update equation is normalized by a diagonal matrix (G) consisting of the initial estimate of the optical properties (μ_0), such that

$$\tilde{J} = JG$$

$G = diag(\kappa; \mu_a)$; Moreover, is implemented in a modified LM algorithm [55], where it is initialized as the variances ratio and is systematically reduced at each iteration (factor of $10^{0.25}$ and scaled by maximum of diagonal of $J^T J$). The iterative procedure is repeated until experimental data matches with modeled data to a tolerance level, which is typically set as 2%.

Once the optical properties are obtained at each wavelength, the chromophore concentrations are calculated using constrained LS fit to the Beer's law relation

$$\mu_a = [\varepsilon]C$$

Where ε is the molar absorption spectra of the tissue's absorbing chromophores and c is the concentration of these chromophores.

The imaging volume for trans-rectal optical tomography can be divided into 2 domains or regions-of-interest (ROIs): the peri-prostate tissue, the prostate. We use soft priori method where the TRUS structural information is utilized to recover absorption coefficients of all the nodes and Jacobian is calculated for every node. The inverse method was tested for two types of reconstruction basis. In first type, the reconstruction basis was separately defined as a mesh other

than the mesh used for FEM field solution whereas in other approach a Cartesian pixel basis [25, 25, 25] was used.

The system utilized steady-state optical tomography reconstruction for absorption tomography**.** The absorption coefficients at the three specific bands ($\mu_a^{\lambda_1}, \mu_a^{\lambda_2}, \mu_a^{\lambda_3}$) were recovered first, then used to calculate the concentrations of HbO and Hb, by

$$\begin{bmatrix} HbO \\ Hb \end{bmatrix}_{2\times1} = \frac{1}{\ln(10)} \cdot \left\{ \frac{1}{[\varepsilon]'[\varepsilon]} \right\}_{2\times2} \cdot [\varepsilon]'_{2\times3} \cdot \begin{bmatrix} \mu_a^{\lambda_1} \\ \mu_a^{\lambda_2} \\ \mu_a^{\lambda_3} \end{bmatrix}$$

Where $[\varepsilon]_{3\times2}$was the matrix of molar extinction coefficients represented by

$$[\varepsilon]_{3\times2} = \begin{bmatrix} \varepsilon_{HbO}(\lambda_1) & \varepsilon_{Hb}(\lambda_1) \\ \varepsilon_{HbO}(\lambda_2) & \varepsilon_{Hb}(\lambda_2) \\ \varepsilon_{HbO}(\lambda_3) & \varepsilon_{Hb}(\lambda_3) \end{bmatrix}$$

Oxy-hemoglobin (HbO), deoxy-hemoglobin (Hb) and water are assumed to be the main absorbers Total hemoglobin is calculated as Hb_T= HbO+Hb (in milliMole), and oxygen saturation as S_tO_2=HbO/Hb_T×100 (in %)

We have used multi-wave length data, which rendered extracting hemoglobin concentration and oxygen saturation information. Conventionally a dual-wavelength combination with one wavelength 10 s of nanometer below and the other wavelength 10 s of nanometer above the isobestic point (805 nm) of hemoglobin could be implemented for extracting the hemoglobin oxygenation information. However, even though two wavelengths in the opposite neighborhoods of the isobestic point were quite accurate in recovering the [Hb_T], they were less reliable in quantifying S_tO_2, which could be attributed partially to the error introduced by neglecting water or lipid [56]. Therefore one additional shorter wavelength 705 nm LD along with the 785 nm LD that is much distant from the isobestic point was implemented to form essentially a three-

wavelength configuration to recover two unknowns of HbO and Hb, as the difference between the absorptions of deoxygenated hemoglobin (Hb) and oxygenated hemoglobin (HbO) became greater toward short-wavelength than in the longer wavelength in the near-infrared band [57], but the limited spectral coverage of the spectrograph-CCD set forced to use an 808 nm LD.

4.3 Continuous Wave Steady-State Measurement

With the development of the analytic or numerical model of the DOT theory, there are several different measurement techniques which have been applied in DOT. The first is time-domain measurement provides information on the increased path length of light in tissue due to multiple scattering events, thus improving the ability to separately recover absorption and scattering properties [58-59]. The second is frequency-domain measurement, when the phase shift of a sinusoidal wave passing through a tissue volume is recorded; provide a less expensive and perhaps stable manner of acquiring time-based information [60-61]. The third one called Continuous Wave steady-state measurement uses the DC light source and directly measure the attenuation of the light power [62-64]. It was applied in the DC-based imaging reconstruction algorithm. Although time-domain and frequency-domain based methods may provide more optical information than CW approaches, a number of researchers have been interested in CW image reconstruction for several years, in part because of the relative simplicity, high signal-to-noise ratio, and low cost of CW techniques [65]. Recent studies have demonstrated that absorption and reduced scattering coefficients can be reconstructed quantitatively from steady-state measurements, to minimize a weighted sum of the squared difference between computed and measured data [66-68].

CHAPTER 5

Results and Discussion

5.1 Image Segmentation

Entire routine is developed using MATLAB. The segmentation results using Snake's algorithm are shown in figure 5.1.

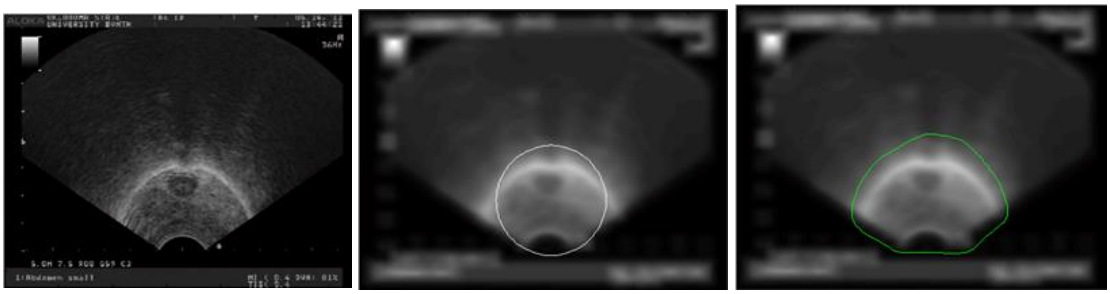

(a) **(b)** **(c)**

Figure 5.1 Snake algorithm (a) TRUS image to be segmented (b) Initialization of Snake (c) image segmentation using Snake

Snake is well suited for images with high contrast and for prostate whose shape and size is known. The Accuracy of Snake depends on complexities in contrast, morphological features and image artifacts. For axial images, Snake may work satisfactorily, but for sagittal images, it is difficult for Snake to segment the prostate accurately. Hence, to obtain more accurate segmentation, selected images are segmented manually.

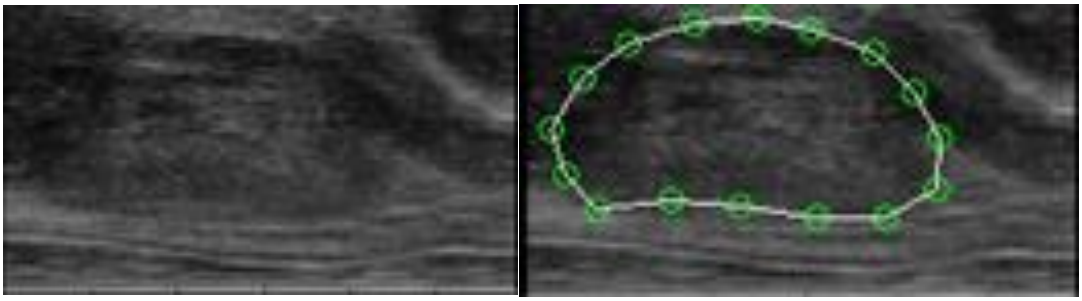

(a) (b)

Figure 5.2 (a) sagittal image (b) Manual Image segmentation for sagittal image

5.2 3D Mesh Profile of a Prostate

A 3D profile of a prostate obtained from a set of 2D TRUS images by manual segmentation is shown in figure 5.3. Mesh density can be selected as per mesh requirements. It is used to guide NIR optical tomography reconstruction. If the mesh is very dense, it takes longer time for reconstruction. However, if the density of the mesh is very less, it affects the reconstruction result. From the simulation results, mesh density shown in 5.3 (b) was selected as a tradeoff between time and accuracy of reconstruction. The Delaunay triangulation in MATLAB gives nodes and elements in the profile. Nodes are the points of the mesh and the elements connect 4 nodes of the tetrahedron.

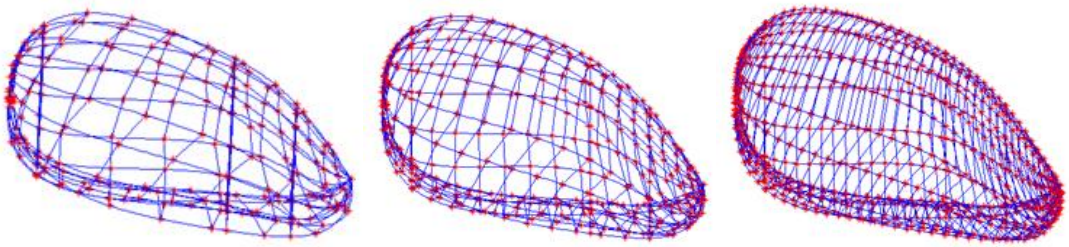

(a) (b) (c)

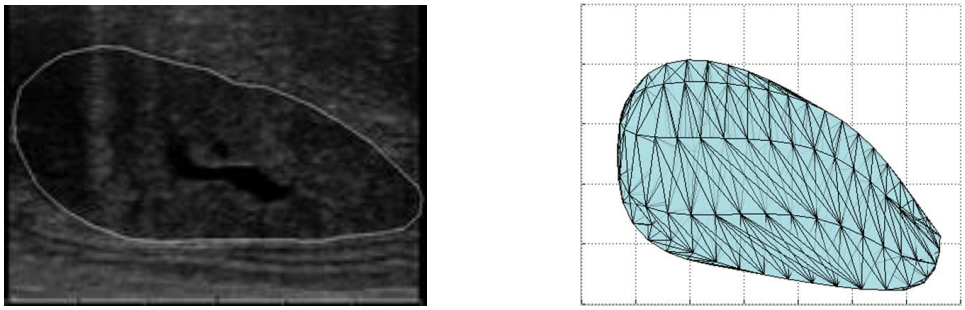

(d) **(e)**

Figure 5.3 (a),(b),(c) meshes with different mesh density, red dots indicate the nodes of a mesh (d) sagittal profile of a prostate, (e) Prostate mesh after Delaunay Triangulation.

The prostate mesh profile after Delaunay triangulation is shown in figure 5.3 (e). We use this prostate mesh as a spatial prior for NIR reconstruction by generating a mesh having a homogenous background region and a prostate region. The NIR image reconstruction uses a 3-dimensional mesh representing 80 x 40 x 70 mm^3 using different optical properties for prostate mesh and homogeneous background mesh as shown in figure 5.4. μ_a value for nodes of homogeneous mesh is 0.008 mm^{-1} whereas, that for nodes of prostate profile mesh is 0.02 mm^{-1}

We perform a soft priori method in which for every node, a Jacobian is calculated and the TRUS structural information is utilized to recover absorption coefficients of all nodes. So, the

hierarchical iteration routine involves 'N' steps where N= no. of nodes. In our case, entire mesh consists of ~9500 nodes. Therefore, their reconstruction took ~5 hours on an Intel Core 2 quad CPU Q8200 at 2.33 GHz processor; 8GB RAM to reconstruct all the absorption and scattering coefficients for one mesh.

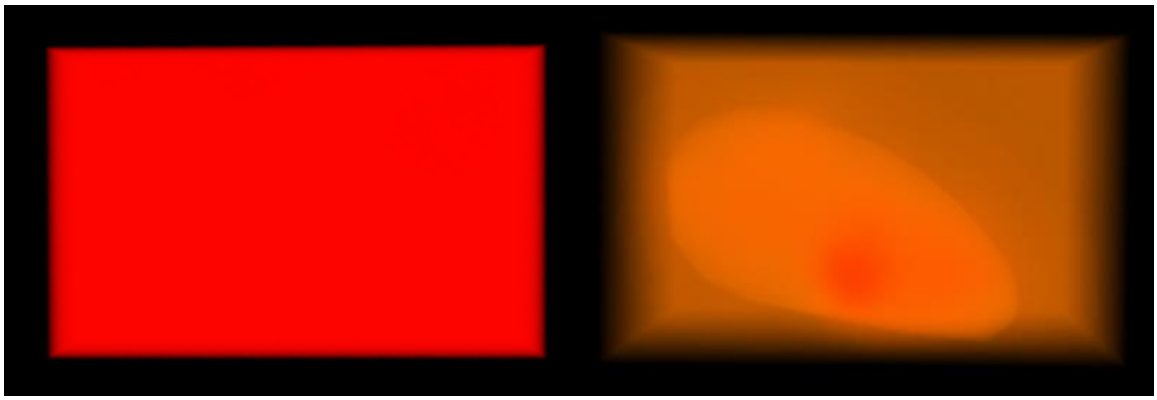

(a) **(b)**

Figure 5.4 absorption coefficient reconstruction for (a) A rectangular mesh without spatial prior (b) homogeneous rectangular mesh using obtained spatial prior

Reconstruction results only for NIRFAST simulation when experimental data is not used are shown in figure 5.5. 1% noise is added to the boundary data. Rectangular mesh without spatial prior cannot differentiate between prostate and the surrounding tissue.

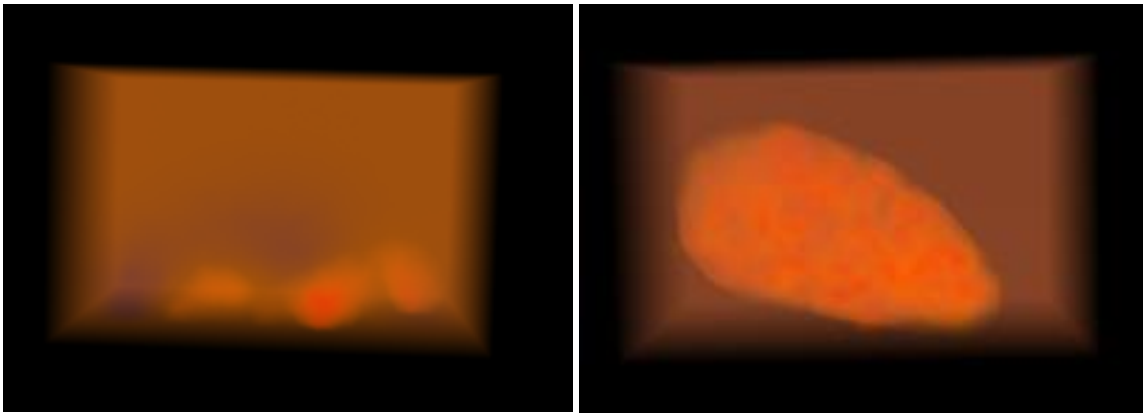

Figure 5.5 absorption coefficient reconstruction for (a) rectangular mesh without spatial prior (b) homogeneous rectangular mesh using obtained spatial prior

Prostate cancer usually appears as an area of abnormal low signal intensity surrounded by the normal homogeneous high signal intensity background of the peripheral zone. Low signal intensity lesions in the peripheral zone display a sensitive but not specific finding for cancer.
The prostate boundary is well-delineated in TRUS, and the spatial extent of a tumor can be defined if it is shown as hypo-echoic on TRUS. This is when the NIR functional contrast can help determine whether a tissue suspicious on US is malignant or not.

The feasibility of obtaining trans-rectal optical tomography of prostate when coupling with TRUS is investigated by simulation. Figure 5.6 and 5.7 show images of grey-scale US, optical tomography of $[Hb_T]$ and S_tO_2 acquired at base-line, days 49, 56 and 63 post-injection, at left-mid-sagittal plane across planned TVT injection site as well as a later developed hypo-echoic mass. Post necropsy pictures are shown to compare the results.

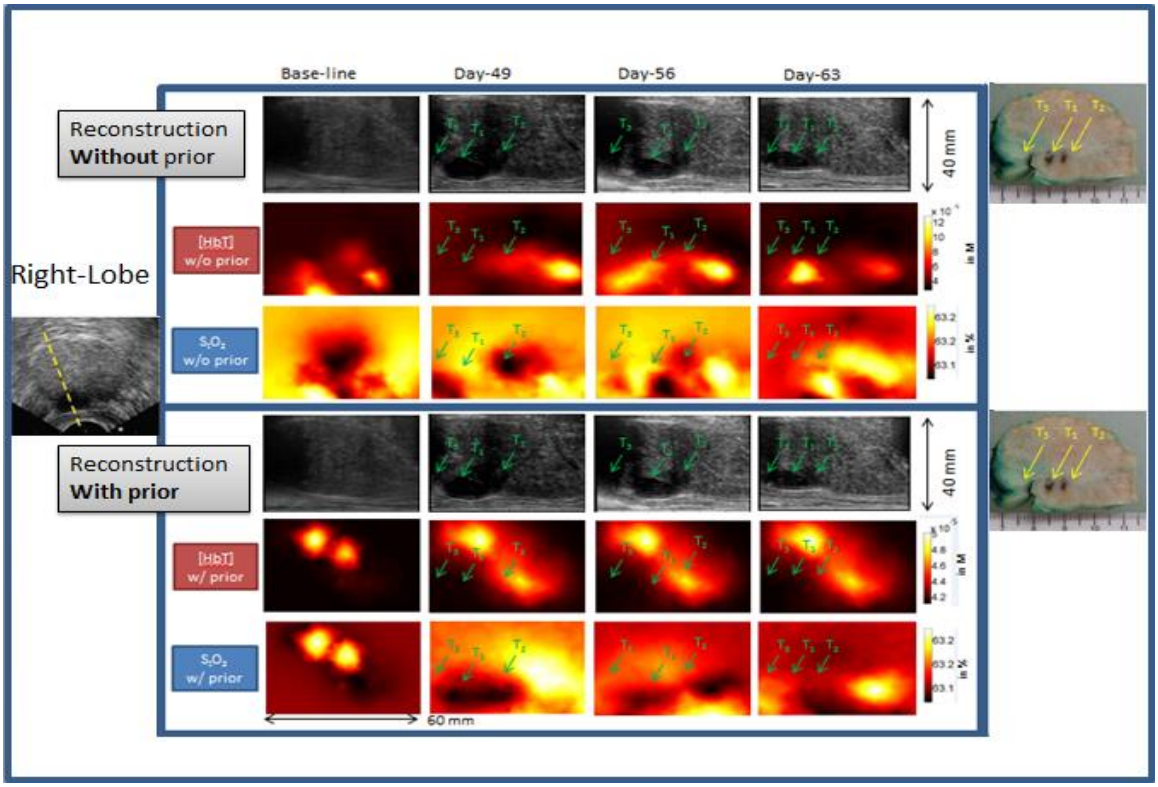

Figure 5.6 Image dimension: 60 mm x 40 mm (cranial-caudal x dorsal-ventral). Images were acquired at base-line, day-49, day-56 and day-63 after the injection, for grey-scale US, $[Hb_T]$ and S_tO_2 (for reconstruction with and without using a spatial prior), at right-mid-sagittal plane across the planed TVT injection site as well as a later developed tumor mass (marked by the dashed line across the axial US image in the lower panel for the right-lobe). The prostate after necropsy was performed is in the right corner. The dashed line at the dorsal edge of the US images indicates the actual location of the NIR sensors at approximately 3 mm ventral to the surface of the US transducer. C indicates cyst; T indicates tumor.

5.3 Baseline

Before TVT injection in a prostate, at baseline, in the left prostatic lobe, a large cystic lesion was observed. It showed highly elevated [Hb_T] and hypoxic for reconstruction with and without spatial prior. Right lobe of the prostate showed homogeneously weak [Hb_T] and S_tO_2 contrast except for some part which shows strong [Hb_T] and hyper-oxic region. The hyperoxic region is believed to be because of the intra-vascular tissue. It can be seen in fig. 5.6 and fig. 5.7

5.4 Right Lobe

After TVT injection in near-cranial-edge of the right lobe, the development of hypo-echoic mass in the middle-aspect of right lobe became evident on US by day 28. By day-49, the mass in the middle aspect of the right lobe which is marked as T_1 and T_2 turned to be an echoic and bi-lobular structure with shadowing at its caudal aspect. The larger dorsal-cranial-mass T_1 had unremarkable [Hb_T] contrast for both with and without spatial prior reconstructions. However, S_tO_2 marked a very strong response for mass T_1 in reconstruction with the spatial prior which was not very well developed in the reconstruction without using spatial prior. The smaller ventral-caudal-mass T_2 had strongly-marked S_tO_2 contrast for both the cases and weakly increased [Hb_T]. The necropsy performed at the end of 63 days showed the presence of tumors T_1, T_2, T_3 which matches our results of hypoxic region.

By day-56, T_1 started regressing and reduced slightly in size on US with echoic reverberation artifact, the hyperoxic focus of it becoming larger, more intense and the [Hb_T] contrast of it remaining undetectable for reconstruction without spatial prior. For reconstruction using spatial prior, T_1 showed hypoxic region comparatively less strong than that for day-49 which is in correspondence with regressed tumor. T_2 was unremarkable on US except for the shadowing hypo-echoic region at the caudal aspect of the previously-indicated mass, the focus of it appearing as slightly hypoxic and having significantly increased [Hb_T] for reconstruction with

spatial prior. Reconstruction without spatial prior showed highly hypoxic response with slightly increased [Hb_T].

By day-63, T_1 remained unchanged in size on US with reduced echoic reverberation artifact, and the caudal aspect of the T_2-indicating region became heterogeneously hypo-echoic without shadowing. The extended region corresponding to T_1 & T_2 was mostly anoxic-like, and only weak hyper-[Hb_T] contrast was observed in the indicated T_2 mass.

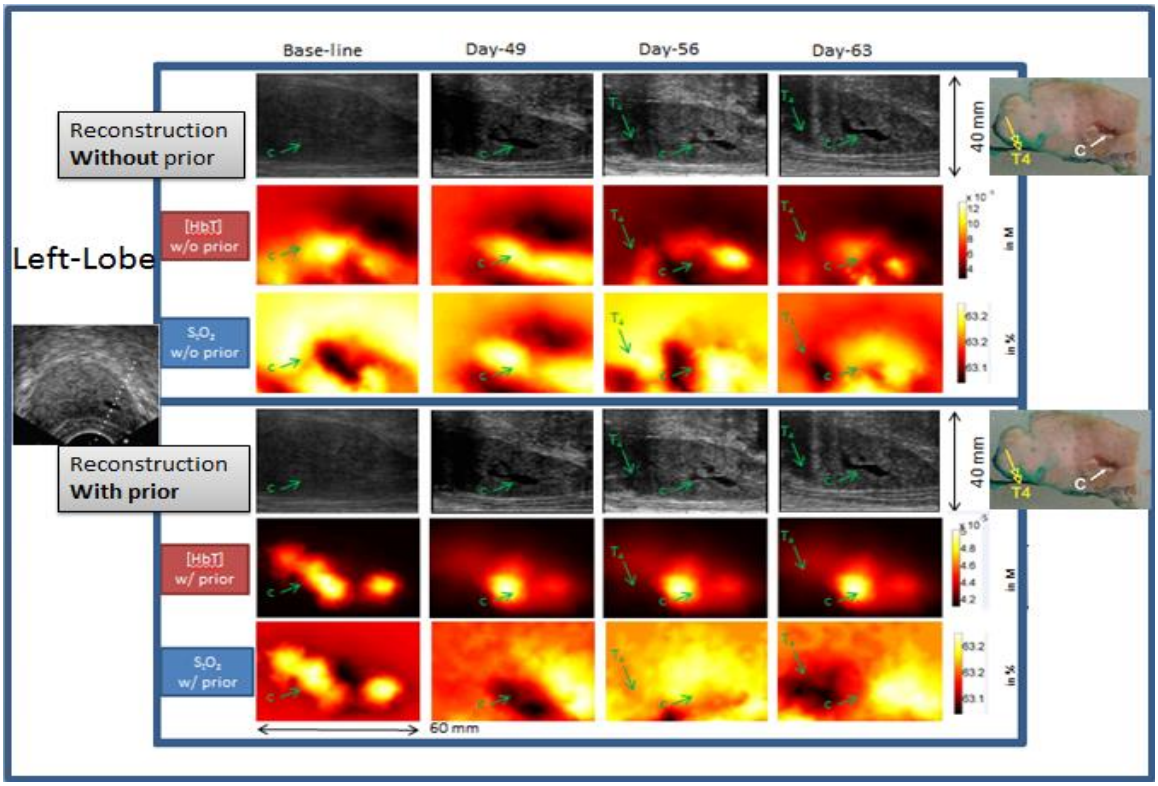

Figure 5.7 Image dimension: 60 mm x 40 mm (cranial-caudal x dorsal-ventral). Images were acquired at base-line, day-49, day-56 and day-63 after the injection, for grey-scale US, [Hb_T] and S_tO_2 (for reconstruction with and without using a spatial prior), at left-mid-sagittal plane across the cyst (marked by the dotted line across the axial US image in the upper panel for the left-lobe) The prostate after necropsy was performed is in the right corner. The dashed line at the dorsal edge of the US images indicates the actual location of

the NIR sensors at approximately 3 mm ventral to the surface of the US transducer. C indicates cyst; T indicates tumor.

5.5 Left Lobe

By day-49 the cystic lesion remained similar in NIR appearances to that in base-line. On Doppler US the blood flow was observed in areas ventral to the cystic lesion. On Doppler US the blood flow was observed in areas ventral to the cystic lesion. The cystic lesion showed strongly elevated [Hb_T] throughout the 63 days of this study for reconstruction using spatial prior in correspondence with the Doppler. However, no consistent feature in the proximity of the cystic lesion indicating lesion-wise blood flow was observed. By day-49, a response at the cystic lesion was highly hypoxic and the shape of the cystic lesion is somewhat visible and both were comparative in size to the ultrasonographically delineated lesion. However, for reconstruction without the spatial prior, cystic lesion showed elevated [Hb_T] similar to that with a spatial prior but, it was shown hyper-oxic in corresponding S_tO_2 map.

By day-56, it presented strong heterogeneously elevated [Hb_T] of which the gross profile resembled the hypoxic profile of the cystic lesion in base-line and day-49. Near that location the corresponding NIR image revealed a cluster of hyper-[Hb_T] region, but the center of which seemed displaced slightly cranially with respect to that of US hypo-echoic mass. The region of strong heterogeneously elevated [Hb_T] was associated with weak heterogeneous hyper-oxia for reconstruction with spatial prior. For reconstruction without spatial prior, cystic lesion was shown highly hypoxic and slightly elevated [Hb_T].

By day-63, the cystic lesion appeared as having weak lesion-wise hyper-[Hb_T] and heterogeneous hyper-oxic interior for reconstruction without using spatial prior whereas, for reconstruction using spatial prior, cystic lesion sows hypoxic interior. The leaked TVT cells from right lobe started to grow in the left lobe in early weeks. In week 4, the tumor mass became big volume at caudal to prostate. By day-63, a hypo-echoic mass with shadowing and Doppler flow-

signal in its caudal aspect was noticed at the cranial-dorsal edge of the left lobe and was seemingly confined within the prostatic capsule which is marked by T_4. At the indicated position of T_4 mass, a hypoxic region of approximately 10 mm in longer axis was seen on S_tO_2 image with weak hyper-[Hb_T] contrast for reconstruction without spatial prior. The same T_4 mass was shown highly hypoxic and weak [Hb_T] for reconstruction with spatial prior. Retrospectively on day-56, the T_4 mass was shown smaller on US with shadowing, and at its dorsal aspect weak [Hb_T] and S_tO_2 contrast were noticed. From all these observations, it can be said that the NIR images reconstructed and displayed at the mid-sagittal plane correlate with TRUS images. The hyper-contrast region of [Hb_T] is correlated with the hypo-echoic region in TRUS images indicating the tumor mass. The necropsy result post 63 days indicates the presence of tumor T_4 was recognized by NIR which did not show up in TRUS images.

Table 5.1

Summary of imaging features observed from T_1.

(Prospectively evaluated)

		Base-line	Day 49	Day 56	Day 63
US-Grey scale		N/A	Anechoic	Anechoic, size reduced	Anechoic, size unchanged
NIR-[Hb_T]	w/ prior w/o prior	N/A N/A	Unremarkable Unremarkable	Unremarkable Hyper, weak	Unremarkable Hyper, weak
NIR- S_tO_2	w/ prior w/o prior	N/A N/A	Strong,hypoxic Unremarkable	Hypoxic, smaller Hyper-oxic	Slightly hypoxic Slightly hypoxic

Table 5.2

Summary of imaging features observed from T_2.

(Prospectively evaluated)

		Base-line	Day 49	Day 56	Day 63
US-Grey scale		N/A	Anechoic	Iso-echoic	Heterogeneously hypo-echoic
NIR-[Hb_T]	w/ prior w/o prior	N/A N/A	Hyper, weak Hyper, weak	Hyper, strong Hyper, weak	Unremarkable Hyper, weak
NIR- S_tO_2	w/ prior w/o prior	N/A N/A	Hypo, strong Hypo, strong	Hypo, weak Hypo, weak	Slightly hypoxic Slightly hyper-oxic

Table 5.3

Summary of imaging features observed from C.

(Prospectively evaluated)

		Base-line	Day 49	Day 56	Day 63
US-Grey scale		Anechoic	Anechoic	Anechoic	Anechoic
NIR-[Hb_T]	w/ prior w/o prior	Hyper, strong Hyper, strong	Hyper, strong Hyper, strong	Hyper, strong Hypo, weak	Hyper, strong Hyper, weak
NIR- S_tO_2	w/ prior w/o prior	Hypo, weak Hypo, strong	Hypo, strong Hyper, strong	Hypo, weak Hypo, weak	indistinct indistinct

Table 5.4

Summary of imaging features observed from T_3.

(Prospectively evaluated)

		Base-line	Day 49	Day 56	Day 63
US-Grey scale		N/A	Hypo-echoic	Hypo-echoic	Hypo-echoic
NIR-[Hb_T]	w/ prior	N/A	Indistinct	Indistinct	Indistinct
	w/o prior	N/A	Indistinct	Hypo, weak	Indistinct
NIR- S_tO_2	w/ prior	N/A	Hypo, strong	Hypo-weak	Hypo-weak
	w/o prior	N/A	Hyper, weak	Hyper, weak	Hypo-weak

Table 5.5

Summary of imaging features observed from T_4.

(Prospectively evaluated)

		Base-line	Day 49	Day 56	Day 63
US-Grey scale		N/A	N/A	Hypo-echoic	Hypo-echoic
NIR-[Hb_T]	w/ prior	N/A	N/A	Indistinct	Indistinct
	w/o prior	N/A	N/A	Indistinct	Indistinct
NIR- S_tO_2	w/ prior	N/A	N/A	Hyper-weak	Hyper-strong
	w/o prior	N/A	N/A	Hyper, strong	Hyper-weak

CHAPTER 6

CONCLUSION AND FUTURE WORK

6.1 Contribution of this work

In summary, sparsely acquired 2D axial TRUS images were successfully segmented to obtain the contour profile of the prostate. Approximate lateral positions of these contours were obtained and this information was used to obtain a 3D profile of a canine prostate under study. A 3D mesh of a canine prostate was generated which was used as a spatial prior in diffuse optical tomography for image reconstruction using soft priori approach in form of regularization. Optical tomography reconstruction was carried out with and without using a structural spatial prior using simulation. Trans-rectal optical tomography was implemented at three wavelength bands to monitor changes of the hemoglobin oxygen saturation (S_tO_2) in addition to those of the total hemoglobin concentration ([Hb_T]) in lesions of a canine prostate, including an induced tumor modeling canine prostate cancer. It was used to validate the three-wavelength NIR imaging of mapping the tissue oxygenation with TVT nodules developed in canine prostate. This work, to our best knowledge, is the first demonstration of TRUS guided NIR image reconstruction for prostate imaging, in vivo.

On US, all the TVT tumor nodules developed during the study were shown to be strongly hypo-echoic that correlated with hypoxic findings on NIR reconstruction images. The cystic lesion had freshly developed blood on its ventral side which was demonstrated correctly by elevated [Hb_T] and hypoxic in images. TRUS coupled optical tomography using structural spatial

prior was shown to enhance the detection of the progression and lateral involvement of the prostatic tumor compared to TRUS coupled optical tomography without using a structural prior. The lesion profiles of T_1, T_2, T_3 and T_4 indicated on S_tO_2 images were comparable to those identified ultrasonographically. For the cyst, the hypoxic region seemed to noticeably outsize the ultrasonographically delineated lesion in some images. This could be due to insufficient image resolution of NIR compared to US or it could also indicate that NIR detection of S_tO_2 characteristics was able to image a peri-cystic tissue non-detectable by ultrasonography.

There are some limitations of this method. We do not see the exact reconstruction at hypo-echoic regions, because, we do not have exact prior for those particular locations of tumor lesions. Some of the tumors may be shown iso-echoic on TRUS, so, the utility or accuracy of this approach is hindered when TRUS images do not specify a suspicious region, or when it is difficult to define the spatial extent of a suspicion region in TRUS.

3D mesh profile generation takes ~1 minute of time after segmented contours are obtained. Reconstruction algorithm takes ~10 hours to simulate on an Intel Core 2 quad CPU Q8200 at 2.33 GHz processor, 8GB RAM, for 10 iterations as we are using soft priori approach where Jacobian is calculated for each node and we have ~9500 nodes.

6.2 Future Work

The results we have here are qualitative. An expert is needed to interpret the results. It is important to prove the presence of malignancy quantitatively. Therefore, next step could be to find solution for quantitative results. We can extract information from TRUS images about the structural spatial priors of hypo-echoic regions so as to get an exact reconstruction at these hypo-echoic regions. If the reconstruction is optimized to reduce the computing time, it is possible to make it a real-time system. The next step could be furthering this research study to additional animal studies and eventually to human prostate cancer study. This approach of using TRUS images can be used to extract structural spatial prior from a human prostate. Prostate trans-rectal

optical imaging is a relatively new area where the initial approach should focus on characterizing the lesions most suspicious to TRUS. Trans-rectal NIR imaging of the lesions suspicious to TRUS or non-suspicious to TRUS is apparently more challenging and should be preceded by trans-rectal NIR/US characterization of a lesion suspicious to US.

REFERENCES

[1] American cancer society: Cancer Facts and Fig. 2011 American Cancer Society, Atlanta, GA 2011

[2] "IARC Worldwide Cancer Incidence Statistics—Prostate". JNCI Cancer Spectrum. Oxford University Press. December 19, 2001. Archived from the original on February 5, 2006. Retrieved on 5 April 2007 through the Internet Archive

[3] Siegel R, (2011). "Cancer statistics, 2011: the impact of eliminating socioeconomic and racial disparities on premature cancer deaths.". CA Cancer J Clin 61: 212–36. doi:10.3322/caac.20121.PMID 21685461.

[4] Baade PD; Youlden DR; Krnjacki LJ (2009 Feb). "International epidemiology of prostate cancer: geographical distribution and secular trends.".Molecular nutrition & food research 53 (2): 171–84.PMID 19101947.

[5] Aumüller, G. (1979). Prostate Gland and Seminal Vesicles. Berlin-Heidelberg: Springer-Verlag.

[6] Moore, K.; Dalley, A. (1999). Clinically Oriented Anatomy. Baltimore, Maryland: Lippincott Williams & Wilkins. ISBN 0-683-06132-1.

[7] American cancer society: Cancer Facts and Fig. 2007 American Cancer Society, Atlanta, GA 2007

[8] Pogue, B.W., et al., Quantitative Hemoglobin Tomography with Diffuse Near-Infrared Spectroscopy: Pilot Results in the Breas T_1. Radiology, 2001. 218(1): p. 261-266.

[9] Ntziachristos, V. and B. Chance, Breast imaging technology: Probing physiology and molecular function using optical imaging - applications to breast cancer. Breast Cancer Res, 2001. 3(1): p. 41 - 46.

[10] Zhu, Q., et al., Imager that combines near-infrared diffusive light and ultrasound. Opt. Lett., 1999. 24(15): p. 1050-1052.

[11] Holboke, M.J., et al., Three-dimensional diffuse optical mammography with ultrasound localization in a human subject. Journal of Biomedical Optics, 2000. 5(2): p. 237-247

[12] Zhen Jiang, G. Reed Holyoak, Kenneth E. Bartels, Jerry W. Ritchey, Guan Xu, Charles F. Bunting, Gennady Slobodov, and Daqing Piao, In vivo trans-rectal ultrasound–coupled optical tomography of a transmissible venereal tumor model in the canine pelvic canal, Journal of Biomedical Optics 030506-3 May/June 2009 Vol. 14.3

[13] Hamid Dehghani, Matthew E. Eames, Phaneendra K. Yalavarthy, Scott C. Davis, Subhadra Srinivasan, Colin M. Carpenter,Brian W. Pogue, Keith D. Paulsen, "Near infrared optical tomography using NIRFAST: Algorithm for numerical model and image reconstruction", Journal: Communications in Numerical Methods in Engineering , vol. 25, no. 6, pp. 711-732, 2009

[14] Hamid Dehghani, , Subhadra Srinivasan, ,Brian W. Pogue, Numerical modelling and image reconstruction in diffuse optical tomography, Phil. Trans. R. Soc. A (2009) 367, 3073–3093 doi:10.1098/rsta.2009.0090

[15] Heng Xu, "MRI-coupled Broadband Near-infrared Tomography for Small Animal Brain Studies" Thayer School of Engineering, Dartmouth College Hanover, New Hampshire May 2005

[16] Jacques, S.L. and B.W. Pogue, Tutorial on diffuse light transport. Journal of Biomedical Optics, 2008. 13(4): p. 041302-19.

[17] Choe, R., et al., Diffuse optical tomography of breast cancer during neoadjuvant chemotherapy: A case study with comparison to MRI. Medical Physics, 2005. 32(4): p. 1128-1139.

[18] Franceschini, M.A., et al., Frequency-domain techniques enhance optical mammography: Initial clinical results. Proceedings of the National Academy of Sciences of the United States of America, 1997. 94(12): p. 6468-6473.

[19] Zhu, Q., et al., Benign versus Malignant Breast Masses: Optical Differentiation with US-guided Optical Imaging Reconstruction1. Radiology, 2005. 237(1): p. 57-66.

[20] Bigler, S.A., R.E. Deering, and M.K. Brawer, Comparison of microscopic vascularity in benign and malignant prostate tissue. Human Pathology, 1993. 24(2): p. 220-226.

[21] Ali, J.H., et al., Near infrared spectroscopy and imaging to probe differences in water content in normal and cancer human prostate tissues. Cancer Res. Treat., 2004. 3: p. 7.

[22] Arnfield, M.R., et al., OPTICAL PROPERTIES OF EXPERIMENTAL PROSTATE TUMORS in vivo. Photochemistry and Photobiology, 1993. 57(2): p. 306-311.

[23] Zhu, T.C., et al., Optical Properties of Human Prostate at 732 nm Measured In Vivo During Motexafin Lutetium–mediated Photodynamic Therapy¶. Photochemistry and Photobiology, 2005. 81(1): p. 96-105.

[24] Svensson, T., et al., In vivo optical characterization of human prostate tissue using near-infrared time-resolved spectroscopy. Journal of Biomedical Optics, 2007. 12(1): p. 014022-10.

[25] Manan, G., et al. Application of Near Infrared Multi-Spectral CCD Imager System to Determine the Hemodynamic Changes in Prostate Tumor. 2006: Optical Society of America.

[26] Liu, H., et al., Noninvasive Investigation of Blood Oxygenation Dynamics of Tumors by Near-Infrared Spectroscopy. Appl. Opt., 2000. 39(28): p. 5231-5243.

[27] Jacques, S.L. and M. Motamedi. Tomographic needles and catheters for optical imaging of prostatic cancer. 1995. San Jose, CA, USA: SPIE.

[28] Musgrove, C., et al. Computational aspects of endoscopic (trans-rectal) near-infrared optical tomography: initial investigations. 2007. San Jose, CA, USA: SPIE.

[29] Piao, D., et al. Near-infrared optical tomography: endoscopic imaging approach. 2007. San Jose, CA, USA: SPIE.

[30] Shweiki, D., Itin, A., Soffer, D., Keshet, E. "Vascular endothelial growth factor induced by hypoxia may mediate hypoxia-initiated angiogenesis." Nature 359, 843-845 (1992).

[31] Kunz, M., Hartmann, A., Flory, E., Toksoy, A., Koczan, D., Thiesen, H. J., Mukaida, N., Neumann, M., Rapp, U. R., Bröcker, E. B., Gillitzer, R. A"noxia-

induced up- regulation of interleukin-8 in human malignant melanoma. A potential mechanism for high tumor aggressiveness." Am J Pathol 155, 753-763 (1999).

[32] Höckel, M., Schlenger, K., Höckel, S., Aral, B., Schäffer, U., Vaupel, P. "Tumor hypoxia in pelvic recurrences of cervical cancer." Int J Cancer 79, 365-369 (1998)

[33] Sundfør, K., Lyng, H., Rofstad, E. K. "Tumour hypoxia and vascular density as predictors of metastasis in squamous cell carcinoma of the uterine cervix." Br J Cancer 78, 822-827 (1998).

[34] Movsas, B., Chapman, J. D., Horwitz, E. M., Pinover, W. H., Green berg, R. E., Hanlon, A. L., Iyer, R., Hanks, G. E. "Hypoxic regions exist in human prostate carcinoma." Urology 53, 11-18 (1999).

[35] Yu, G., Durduran, T., Zhou, C., Zhu, T. C., Finlay, J. C., Busch, T. M., Malkowicz, S. B., Hahn, S. M., Yodh, A. G. "Real-time in situ monitoring of human prostate photodynamic therapy with diffuse light." Photochem Photobiol 82, 1279-1284 (2006).

[36] Leith, J. T., Quaranto, L., Padfield, G., Michelson, S., Hercbergs, A. "Radiobiological studies of PC-3 and DU-145 human prostate cancer cells: x-ray sensitivity in vitro and hypoxic fractions of xenografted tumors in vivo." Int J Radiat Oncol Biol Phys 25, 283-287 (1993).

[37] Vukanovic, J., Isaacs, J. T. "Human prostatic cancer cells are sensitive to programmed (apoptotic) death induced by the antiangiogenic agent linomide." Cancer Res 55, 3517-3520 (1995).

[38] Tatum, J. L., Kelloff, G. J., Gillies, R. J., Arbeit, J. M., Brown, J. M., 11. Chao, K. S., Chapman, J. D., Eckelman, W. C., Fyles, A. W., Giaccia, A. J., Hill, R. P., Koch, C. J., Krishna, M. C., Krohn, K. A., Lewis, J. S., Mason, R. P., Melillo, G., Padhani, A. R., Powis, G., Rajendran, J. G., Reba, R., Robinson, S. P., Semenza, G. L., Swartz, H. M., Vaupel, P., Yang, D., Croft, B., Hoffman, J., Liu, G., Stone, H., Sullivan, D. "Hypoxia: importance in tumor biology, noninvasive measurement by imaging, and value of its measurement in the management of cancer therapy." Int J Radiat Biol 82, 699-757 (2006). Review.

[39] Li, C., et al., Using a priori structural information from magnetic resonance imaging to investigate the feasibility of prostate diffuse optical tomography and spectroscopy: A simulation study. Medical Physics, 2007. 34(1): p. 266-274.

[40] B.W. Pogue et al., "Near-infrared diffuse tomography with a priori MRI structural information: Testing a hybrid image reconstruction methodology with functional imaging of the rat cranium," in Proc. SPIE Conf., vol. 3597, 1999, p. 484.

[41] Brooksby, B.A., et al., Near-infrared (NIR) tomography breast image reconstruction with a priori structural information from MRI: algorithm development for reconstructing heterogeneities. Selected Topics in Quantum Electronics, IEEE Journal of, 2003. 9(2): p. 199-209.

[42] Jiang, Z., et al., Trans-rectal ultrasound-coupled near-infrared optical tomography of the prostate, Part II: Experimental demonstration. Opt. Express, 2008. 16(22): p. 17505-17520

[43] Niu, H., et al., Development of a compensation algorithm for accurate depth localization in diffuse optical tomography. Opt. Lett., 2010. 35(3): p. 429-431.

[44] D. Shen, Y. Zhan, and C. Davatzikos, Segmentation of prostate boundaries from ultrasound images using statistical shape model, IEEE Trans. Med. Imag., vol. 22, no. 4, pp. 539–551, 2003.

[45] S.D. Pathak, D.R. Haynor, and Y. Kim, Edge-guided boundary delineation in prostate ultrasound images, IEEE Trans. Med. Imag., vol. 19, no. 12, pp. 1211–1219, 2000.

[46] F. Zhao and C.J.S. deSilva, Contour extraction in prostate ultrasound images using the wavelet transform and snakes, Proc. Intl. Conf. Eng. Med. Bio., vol. 3, pp. 2641–2644, 2001.

[47] S. Ghose, A. Oliver, R. Marti, X. Llad´o, J. Freixenet, J. C. Vilanova, F. Meriaudeau, A Probabilistic Framework For Automatic Prostate Segmentationwith A Statistical Model Of Shape And Appearance, 2011 18th IEEE International Conference on Image Processing

[48] Liu YJ, Ng WS, Teo MY, Lim HC. Computerized prostate boundary estimation in ultrasound images using the radial bas-relief method. Med Biol Eng Comput 1997; 35:4450–4454.

[49] S.S. Mohamed, T.K. Abdel-galil, M.M.A. Salma, A. Fenster, D.B. Downey, and K. Rizkalla, "Prostate cancer diagnosis based on gabor filter texture segmentation of ultrasound image," IEEE CCECE, pp. 1485–1488, 2003

[50] Michael Kass, Andrew Witkin, and Demetri Terzopoulos, "Snakes: Active Contour Models", International Journal of Computer Vision, 321-331 (1988).

[51] Z. Jiang, D. Piao, K. E. Bartels, G. R. Holyoak, J. W. Ritchey, C. L. Ownby, K. Rock, G. Slobodov, "Transrectal Ultrasound-Integrated Spectral Optical Tomography of Hypoxic Progression of a Regressing Tumor in a Canine

Prostate" Technology in Cancer Research and Treatment ISSN 1533-0346 Volume 10, Number 6, December 2011

[52] Daqing Piao, Kenneth E. Bartels, Zhen Jiang, Gilbert Reed Holyoak, Jerry W. Ritchey, Guan Xu, Charles F. Bunting, Member, IEEE, and Gennady Slobodov, "Alternative Transrectal Prostate Imaging: A Diffuse Optical Tomography Method", IEEE Journal Of Selected Topics In Quantum Electronics, Vol. 16, No. 4, July/August 2010

[53] Hamid Dehghani, Subhadra Srinivasan, Brian W. Pogue And Adam Gibson," Numerical Modeling And Image Reconstruction In Diffuse Optical Tomography", Phil. Trans. R. Soc. A (2009) 367, 3073–3093

[54] Pogue, B.W., et al., Three-Dimensional Simulation of Near-Infrared Diffusion in Tissue: Boundary Condition and Geometry Analysis for Finite-Element Image Reconstruction. Appl. Opt., 2001. 40(4): p. 588-600.

[55] Schweiger, M., S.R. Arridge, and D.T. Delpy, Application of the finite-element method for the forward and inverse models in optical tomography. Journal of Mathematical Imaging and Vision, 1993. 3(3): p. 263-283.

[56] Zhu, Q. Optical tomography with ultrasound localization: initial clinical results and technical challenges. *Technol Cancer Res Treat 4*, 235-244 (2005).

[57] Jiang, Z., Piao, D., Holyoak, G. R., Ritchey, J. W., Bartels, K. E., Slobodov, G., Bunting, C. F., Krasinski, J. S. Trans-rectal ultrasound-coupled spectral optical tomography of total hemoglobin concentration enhances assessment of the laterality and progression of a transmissible venereal tumor in canine prostate. *Urology 77*, 237-242 (2011).

[58] M. S. Patterson, Chance B., Wilson, B. C., "Time resolved reflectance and transmittances for the non-invasive measurement of tissue optical properties," Appl. Opt. 28, 2331-2336 (1989).

[59] B. Chance, Nioka, S., Kent, J., McCully, K., Fountain, M., Greenfield, R., Holtom, G., "Time-resolved spectroscopy of hemoglobin and myoglobin in resting and ischemic muscle," Analy. Biochem. 174, 698-707 (1988).

[60] M. S. Patterson, Moulton, J. D., Wilson, B. C., Berndt, K. W., Lakowicz, J. R., "Frequency-domain reflectance for the determination of the scattering and absorption properties of tissue," Appl. Opt. 30, 4474-4476 (1991).

[61] J. Fishkin, Gratton, E., van de Ven, M. J., Mantulin, W. W., "Diffusion of intensity modulated near infrared light in turbid media," Proc. SPIE 1431, 122-135 (1991).

[62] X. Zhou and T. C. Zhu, "Image reconstruction of continuous wave diffuse optical tomography (DOT) of human prostate," in Proc. the COMSOL Users Conference (2006) .

[63] D. Piao, H. Xie. W. Zhang, J. S. Kransinski, G. Zhang, H. Dehghani, and B. W. Pogue, ―Endoscopic, rapid near-infrared optical tomography,‖ Opt. Lett. 31, 2876-2878 (2006).

[64] N. Iftimia and H. Jiang, ―Quantitative optical image reconstruction of turbid media by use of direct-current measurements,‖ Appl. Opt. 39, 5256-5261 (2000).

[65] Z. Yuan, Q. Zhang, E. Sobel, and H. Jiang, ―Three-dimensional diffuse optical tomography of osteoarthritis: initial results in the finger joints,‖ J. Biomed. Opt. 12, 034001 (2007).

[66] Y. Xu, X.Gu, T. Khan and H. Jiang, ―Absorption and scattering images of heterogeneous scattering media can be simultaneously reconstructed by use of dc data‖, Applied Optics, Vol.41, No.25, Sep. 1, 2002.

[67] Xu G, Piao D, Musgrove CH, Bunting CF, Dehghani H, ―Trans-rectal ultrasound-coupled near-infrared optical tomography of the prostate Part I: Simulation,‖ Optics Express, Vol. 16, Iss. 22, pp. 17484–17504 (2008).

[68] Zhang A, Piao D, Bunting CF, Pogue BW, ―Photon diffusion in a homogeneous medium bounded externally or internally by an infinitely long circular cylindrical applicator ---- Part I: steady-state theory,‖ Journal of Optical Society of America, A, Vol. 27, No. 3, pp. 648-662 (2010).

[69] Hamid Dehghani1,2, Colin M. Carpenter2, Phaneendra K. Yalavarthy2, Brian W. Pogue2, And Joseph P. Culver3, Structural A-Priori Information In Near Infrared Optical Tomography, Proc. Of Spie Vol. 6431 64310b-2

[70] Daqing Piao, Zhen Jiang, Kenneth E. Bartels, G. Reed Holyoak, Jerry W. Ritchey, Guan Xu, Charles F. Bunting And Gennady Slobodov, In Vivo Trans-Rectal Ultrasound-Coupled Near-Infrared Optical Tomography Of Intact Normal Canine Prostate, Journal Of Innovative Optical Health Sciences Vol. 2, No. 3 (2009) 215–22

[71] Zhen Jiang, D. Piao, G. R. Holyoak, J. W. Ritchey, K. E. Bartels, G. Slobodov, C. F. Bunting, And J. S. Krasinski, Trans-Rectal Ultrasound–Coupled Spectral Optical Tomography Of Total Hemoglobin Concentration Enhances Assessment Of The Laterality And Progression Of A Transmissible Venereal Tumor In Canine Prostate, Urology Xx: Xxx, Xxxx.© 2010 Elsevier Inc.

[72] Soumya Ghose, Arnau Oliver, Robert Mart'i, Xavier Llad'o, Jordi Freixenet, Jhimli Mitra, Joan C. Vilanova, Josep Comet and Fabrice Meriaudeau, Statistical Shape and Probability Prior Model for Automatic Prostate Segmentation, 2011

International Conference on Digital Image Computing: Techniques and Applications.

[73] Vincent Chan and Anahi Perlas , Basics of Ultrasound Imaging, S.N. Narouze (ed.), Atlas of Ultrasound-Guided Procedures in Interventional Pain Management, DOI 10.1007/978-1-4419-1681-5_2, © Springer Science+Business Media, LLC 2011

[74] Zhen Jiang, Daqing Piao, Guan Xu, Jerry W. Ritchey, G. Reed Holyoak, Kenneth E. Bartels, Charles F. Bunting,1 Gennady Slobodov, Jerzy S. Krasinki, Trans-rectal ultrasound-coupled near-infrared optical tomography of the prostate Part II: Experimental demonstration, 27 October 2008 / Vol. 16, No. 22 / OPTICS EXPRESS 17506

[75] S. S. Mohamed, T. K. Abdel-galil, M. M. A. salama, A. Fenster, D. B. Downey, and K. Rizkalla, E. F. El-saadany, and M. kame1, prostate cancer diagnosis based on Gabor filter texture segmentation of ultrasound image, CCECE 2003 - CCGEI 2003, Montrial, May/mai 2003 0 7803-7781-8/03/$17.00 0 2003 IEEE

[76] Ang Li, Eric L. Miller, Misha E. Kilmer, Thomas J. Brukilacchio, Tina Chaves, Jonathan Stott, Quan Zhang, Tao Wu, MaryAnn Chorlton, Richard H. Moore, Daniel B. Kopans, and David A. Boas, Tomographic optical breast imaging guided by three-dimensional mammography, September 2003 _ Vol. 42, No. 25 _ APPLIED OPTICS

[77] LAURENCE R. WATSON, RDMS, Ultrasound Anatomy for Prostate Brachytherapy, Seminars in Surgical Oncology 1997; 13:391–398

[78] Ang Li, Greg Boverman, Yiheng Zhang, Dana Brooks, Eric L. Miller, Misha E. Kilmer, Quan Zhang, Elizabeth M. C. Hillman, and David A. Boas, Optimal linear inverse solution with multiple priors in diffuse optical tomography, APPLIED OPTICS _ Vol. 44, No. 10 _ 1 April 2005

[79] Ladak HM, Mao F, Wang YQ, et al. Prostate segmentation from 2D ultrasound images. Med Phys 2000; 27:1777–1788.

[80] M. J. Holboke, Bruce J. Tromberg, X. Li, N. Shah, J. Fishkin, D. Kidney, J. Butler, Britton Chance, Arjun G. Yodh, Three-dimensional diffuse optical mammography with ultrasound localization in a human subject, Journal of Biomedical Optics. 5(2), 237 (Apr 01 2000); doi: 10.1117/1.429992

[81] Janssen, H. L., Haustermans, K. M., Balm, A. J., Begg, A. C. "Hypoxia in head and neck cancer: how much, how important?" Head Neck 27, 622-638 (2005). Review.

APPENDICES

MATLAB soft codes

Manual segmentation for prostate segmentation-	contourTracking.m
Obtain points inside the prostate blob-	meshInside.m
Get 3D mesh profile-	tetra_mesh_try.m
Find approximate plane position-	widthDist.m
Reconstruction algorithm-	recon_week7.m
Show tomographic results-	showresults_no_priori.m
Quantify oxygen content-	try_quant.m

contourTracking.m

```
% code for Manual contour tracking for prostate segmentation

clc; clear all; close all;

kkk=imread('d4w9cranial3.png'); %read image
imagesc(kkk);
colormap(gray);
[x y]=getpts;   %get input points from user
P1=[x(:) y(:)];
hold on
% scatter(P1(:,1),P1(:,2),'g');
P1=[P1; P1(1,:)];
xe1=[P1(:,1); P1(1,1)];
ye1=[P1(:,2); P1(1,2)];
plot(xe1,ye1,'w');
hold off;
P1=[P1 210*ones(length(P1),1)];     % get 3rd dimension using widthDist program
% follow the same for 2nd axial image
kkk=imread('d4w9cranial6.png');
figure
imagesc(kkk);
colormap(gray);
[x y]=getpts;
P2=[x(:) y(:)];
hold on
% scatter(P(:,1),P(:,2),'g');
P2=[P2; P2(1,:)];
xe2=[P2(:,1); P2(1,1)];
ye2=[P2(:,2); P2(1,2)];
plot(xe2,ye2,'w');
hold off;
P2=[P2 375*ones(length(P2),1)];

% follow the same for 3rd axial image
kkk=imread('d4w9cranial8.png');
figure
imagesc(kkk);
colormap(gray);
[x y]=getpts;
P3=[x(:) y(:)];
hold on
% scatter(P(:,1),P(:,2),'g');
P3=[P3; P3(1,:)];
xe3=[P3(:,1); P3(1,1)];
ye3=[P3(:,2); P3(1,2)];
plot(xe3,ye3,'w');
hold off;
P3=[P3 430*ones(length(P3),1)];

%   follow the same for sagittal image
```

```
kkk=imread('Left_mid_mid.png');
figure
imagesc(kkk);
colormap(gray);
[x y]=getpts;
P4=[x(:) y(:)];
hold on
% scatter(P(:,1),P(:,2),'g');
P4=[P4; P4(1,:)];
xe4=[P4(:,1); P4(1,1)];
ye4=[P4(:,2); P4(1,2)];
plot(xe4,ye4,'w');
P4=[P4 300*ones(length(P4),1)];
hold off
figure
hold on

plot3(P1(:,3),P1(:,2),P1(:,1),'b');
plot3(P2(:,3),P2(:,2),P2(:,1),'b');
plot3(P3(:,3),P3(:,2),P3(:,1),'b');
plot3(P4(:,1),P4(:,2),P4(:,3),'r');

hold off
% save all co-ordinates
save d4w8P1 P1
save d4w8P2 P2
save d4w8P3 P3
save d4w8P4 P4


meshInside.m
% create mesh inside profile
% nodes: (px,py,pz),
% (ipx_full,ipy_full,ipz_full),ran_points,ran_points1(k,:),[X1 Y1 Z1],[X2
% Y2 Z2],[X3 Y3 Z3]
% clc; clear all;
close all;
% load d4w8P1;load d4w8P2;load d4w8P3

figure; rotate3d on; hold on; view(270,180)

% plot3(P1(:,3),P1(:,2),P1(:,1),'b.');
% plot3(P2(:,3),P2(:,2),P2(:,1),'b.');
% plot3(P3(:,3),P3(:,2),P3(:,1),'b.');
% drawnow; pause(0.2);

% create intermediate mesh on surface
cranial_mean=mean(P3);
caudal_mean=mean(P1);
interPt=[];
for i=1:length(P1)
```

```
    pz = [caudal_mean(1,1) P1(i,1) P2(i,1) P3(i,1) cranial_mean(1,1)];
    py = [caudal_mean(1,2)-50 P1(i,2) P2(i,2) P3(i,2) cranial_mean(1,2)];
    px = [caudal_mean(1,3)-20 P1(i,3) P2(i,3) P3(i,3) cranial_mean(1,3)+50];
    pt = interparc(200,px,py,pz);
    interPt=[interPt; pt];
    % Plot the result
    plot3(px,py,pz,'r*',pt(:,1),pt(:,2),pt(:,3),'b');
%         drawnow; pause(0.1);
end

n=0:5:length(pt);
ipx_full=[]; ipy_full=[]; ipz_full=[];
for j=1:length(n)
    ipx=[];    ipy=[];    ipz=[];
    for i=1:30
        ipx=[ipx interPt(n(j)+200*i,1)];
        ipy=[ipy interPt(n(j)+200*i,2)];
        ipz=[ipz interPt(n(j)+200*i,3)];
    end
    ipx=[ipx ipx(1)];
    ipy=[ipy ipy(1)];
    ipz=[ipz ipz(1)];
    for i=1:length(ipx)-1
        line([ipx(1,i) ipx(1,i+1)],[ipy(1,i) ipy(1,i+1)],[ipz(1,i) ipz(1,i+1)]);
    end
    plot3(ipx,ipy,ipz);
    ipx_full=[ipx_full; ipx];
    ipy_full=[ipy_full; ipy];
    ipz_full=[ipz_full; ipz];
end
% hold off
% figure
% hold on
% for i=1:length(ipx_full)
%     plot3(ipx_full(i,:),ipy_full(i,:),ipz_full(i,:),'g.');
%     drawnow; pause(0.2);
% end
% plot3(mean2(ipx_full),mean2(ipy_full),mean2(ipz_full),'r.');
% drawnow; pause(0.2);
% % find mid point
%
[m n]=size(ipx_full);
k=1;
for i=1:m
    for j=1:2:n
% for points at regular intervals
        ran_points(k,:)= [(mean2(ipx_full)+ipx_full(i,j))/2 (mean2(ipy_full)+ipy_full(i,j))/2
(mean2(ipz_full)+ipz_full(i,j))/2];
        ran_points1(k,:)= [(ran_points(k,1)+ipx_full(i,j))/2 (ran_points(k,2)+ipy_full(i,j))/2
(ran_points(k,3)+ipz_full(i,j))/2];
        k=k+1;
```

```
   end
end

k=1;
for i=1:2:m
   for j=1:2:n
      ip_single(k,1)=ipx_full(i,j);
      ip_single(k,2)=ipy_full(i,j);
      ip_single(k,3)=ipz_full(i,j);
      k=k+1;
   end
end

% create mesh around profile

meanP2=mean(P2);

x = meanP2(1)-40:20:meanP2(1)+40; % width 8
y = meanP2(2)-30:20:meanP2(2)+30; % length 6
z = meanP2(3)-35:20:meanP2(3)+35; % height 7

[X1 Y1 Z1] = meshgrid(x([1 end]),y,z);
[X2 Y2 Z2] = meshgrid(x,y([1 end]),z);
[X3 Y3 Z3] = meshgrid(x,y,z([1 end]));

h = plot3([X1(:);X2(:);X3(:)], [Y1(:);Y2(:);Y3(:)], [Z1(:);Z2(:);Z3(:)],'.');
set(h, 'Color',[0.5 0.5 1], 'LineWidth',1)

xlabel('8 units');
ylabel('6 units');
zlabel('7 units');
axis off
view(3), axis vis3d
camproj perspective, rotate3d on
axis on
hold off

tetra_mesh_try.m
% form a mesh in a tetrahedron form
meshInside
load mesh_f_mesh_nodes;

outer_fwd_mesh=[];
outer_fwd_mesh=zee(:,2:end);
clc; close all;
% only for prostate profile
x_coord=[ip_single(:,1);ran_points(:,1);ran_points1(:,1)]/5-30;
y_coord=max(outer_fwd_mesh(:,2))-[ip_single(:,2);ran_points(:,2);ran_points1(:,2)]/5+10;
z_coord=max(outer_fwd_mesh(:,3))-[ip_single(:,3);ran_points(:,3);ran_points1(:,3)]/5+40;
% % for profile blob with outer mesh
%
```

```
% x_pros=[ip_single(:,1); ran_points(:,1); ran_points1(:,1)]/5-30;
% y_pros=max(outer_fwd_mesh(:,2))-[ip_single(:,2); ran_points(:,2); ran_points1(:,2)]/5+10;
% z_pros=max(outer_fwd_mesh(:,3))-[ip_single(:,3); ran_points(:,3); ran_points1(:,3)]/5+40;
%
% x_coord=[x_pros;outer_fwd_mesh(:,1)];
% y_coord=[y_pros;outer_fwd_mesh(:,2)];
% z_coord=[z_pros;outer_fwd_mesh(:,3)];

x = x_coord;                % x data
y = z_coord;                % y data
z = y_coord;                % z data
tri = delaunay(x,y);            % Create a 2-D triangular mesh
figure
hold on
grid;
tri_rotate=trimesh(tri,x,y,z);              % Plot the mesh in 3-D
hold off
figure
hold on
grid on;
tri3 = delaunay3(x,y,z);            % Create a 3-D triangular mesh
faceColor  = [0.6875 0.8750 0.8984];
tetramesh(tri3,[x(:) y(:) z(:)],'FaceColor', faceColor,'FaceAlpha',0.5);
hold off
xyz=[x y z];
nodes_intern=zeros(length(xyz),1);
nodes_mesh=[nodes_intern];
nodes_mesh=[nodes_mesh xyz];
param_intern=[];
% for i=1:length(nodes_intern)
for i=1:length(xyz)
   param_intern=[param_intern; [0.008 0.330688 1.33  ] ];
end
param_extern=[];
for i=1:length(nodes_extern)
   param_extern=[param_extern; [0.007 0.331016 1.33 ]];
end
param_mesh=[param_intern;param_extern];
elem_mesh=tri3+length(outer_fwd_mesh);

widthDist.m
% find distance to locate view position

clc; clear all; close all;
figure;
kkk=imread('d4w8cranial_1.png');
imagesc(kkk);
colormap(gray);
[x1 y1]=getpts;
pros_width(1) = sqrt((x1(1)-x1(2))^2 + (y1(1)-y1(2))^2);
hold on
```

```
scatter(x1,y1,'w');
plot(x1,y1,'y');
hold off

figure
kkk=imread('d4w8cranial_3.png');
imagesc(kkk);
colormap(gray);
[x2 y2]=getpts;
pros_width(2) = sqrt((x2(1)-x2(2))^2 + (y2(1)-y2(2))^2);
hold on
scatter(x2,y2,'w');
plot(x2,y2,'y');
hold off

figure
kkk=imread('d4w8cranial_5.png');
imagesc(kkk);
colormap(gray);
[x3 y3]=getpts;
pros_width(3) = sqrt((x3(1)-x3(2))^2 + (y3(1)-y3(2))^2);
hold on
scatter(x3,y3,'w');
plot(x3,y3,'y');
hold off


pros_width

figure;
kkk=imread('Left_mid_8.png');
imagesc(kkk);
colormap(gray);
[x y]=getpts;
pros_sagi(1) = sqrt((x(1)-x(2))^2 + (y(1)-y(2))^2);
pros_sagi(2) = sqrt((x(3)-x(4))^2 + (y(3)-y(4))^2);
pros_sagi(3) = sqrt((x(5)-x(6))^2 + (y(5)-y(6))^2);
pros_sagi
```

recon_week7.m

```
% reconstruction routine for week 7
clear; clc; close all;
%% Get background data
mesh_f_pros='mesh_combined_wo_prior';
mesh_r_pros='mesh_r_mesh';

load('roi_04_06_shift_96.mat');
for c_i=1:1
   switch c_i

      case {1}
```

```
            content='Left_mid_';
            mi=5;
        case {2}
            content='Right_mid_mid_';
            mi=2;
    end;
    for meas_i=1:1

        out_fn_1=strcat(content,num2str(meas_i),'_1_out');
        regular=1;
        [mesh,pj_error,it] =
reconstruct_stnd_0(mesh_f_pros,mesh_r_pros,0,'w1.paa',10,regular,out_fn_1,0);
        while it<3
            regular=2*regular;
            [mesh,pj_error,it] =
reconstruct_stnd_0(mesh_f_pros,mesh_r_pros,0,'w1.paa',10,regular,out_fn_1,0);
        end;
        clear mesh;

        out_fn_2=strcat(content,num2str(meas_i),'_2_out');
        regular=1;
        [mesh,pj_error,it] =
reconstruct_stnd_0(mesh_f_pros,mesh_r_pros,0,'w2.paa',10,regular,out_fn_2,0);
        while it<3
            regular=2*regular;
            [mesh,pj_error,it] =
reconstruct_stnd_0(mesh_f_pros,mesh_r_pros,0,'w2.paa',10,regular,out_fn_2,0);
        end;
        clear mesh;

        out_fn_3=strcat(content,num2str(meas_i),'_3_out');
        regular=1;
        [mesh,pj_error,it] =
reconstruct_stnd_0(mesh_f_pros,mesh_r_pros,0,'w3.paa',10,regular,out_fn_3,0);
        while it<3
            regular=2*regular;
            [mesh,pj_error,it] =
reconstruct_stnd_0(mesh_f_pros,mesh_r_pros,0,'w3.paa',10,regular,out_fn_3,0);
        end;
        clear mesh;

    end;
end;

showresults_no_priori.m
clear; clc; close all;
mesh_f_pros='mesh_combined_wo_prior';
data_meas_fn='Left_mid_1';
out_fn_1=strcat(data_meas_fn,'_1_out');
out_fn_2=strcat(data_meas_fn,'_2_out');
out_fn_3=strcat(data_meas_fn,'_3_out');
```

```
level=35;
mesh_1 = read_solution(mesh_f_pros,out_fn_1); %705nm
close all;
rasterize_mua(mesh_1,'y',level);
mesh_2 = read_solution(mesh_f_pros,out_fn_2); %785nm
close all;
rasterize_mua(mesh_2,'y',level);
mesh_3 = read_solution(mesh_f_pros,out_fn_3); %808nm
close all;
rasterize_mua(mesh_3,'y',level);mua_1=mesh_1.mua; mua_2=mesh_2.mua;
mua_3=mesh_3.mua;

% e_1: 704nm, e_2:784nm, e_3: 806nm; from human blood;
e_1_hbo_human=298/10*log(10);
e_1_hb_human=1687.76/10*log(10);
e_2_hbo_human=730.8/10*log(10);
e_2_hb_human=996.72/10*log(10);
e_3_hbo_human=844/10*log(10);
e_3_hb_human=730.28/10*log(10);


% e_1_hbo=600/10*log(10);
% e_1_hb=1100/10*log(10);
% e_2_hbo=800/10*log(10);
% e_2_hb=900/10*log(10);
% e_3_hbo=844/10*log(10);
% e_3_hb=730.28/10*log(10);

e_1_hbo=e_1_hbo_human;
e_1_hb=e_1_hb_human;
e_2_hbo=e_2_hbo_human;
e_2_hb=e_2_hb_human;
e_3_hbo=e_3_hbo_human;
e_3_hb=e_3_hb_human;

extc_3=[e_1_hbo e_1_hb; e_2_hbo e_2_hb; e_3_hbo e_3_hb];

clear e_1_* e_2_* e_3_*;

F=[mua_1'; mua_2'; mua_3'];
Hb_both=(extc_3'*extc_3)\extc_3'*F;

hbo=Hb_both(1,:)';
hb=Hb_both(2,:)';

HbT=hbo+hb;
StO2=hbo./HbT*100;

mesh=load_mesh(mesh_f_pros);
mesh.mua=HbT;
rasterize_mua(mesh,'y',level);
```

```
mesh.mua=StO2;
rasterize_mua(mesh,'y',level);

try_quant.m
close all; clc; clear all;
mesh=load_mesh('mesh_f_mesh');
xxyz=mesh.nodes;
roi_index=[];
index=0;
roi=[15,15,15];
for i=1:length(xxyz)
   find_dist=sqrt((roi(1,1)-xxyz(i,1))^2 + (roi(1,2)-xxyz(i,2))^2 +(roi(1,3)-xxyz(i,3))^2);
   if (find_dist)<5
      index=index+1;
      roi_index(index)=i;

   end
end

for i=1:length(roi_index)
   load('sto2_7.mat')
   roi_sto2_7(i)=StO2(roi_index(i));
   load('sto2_8.mat')
   roi_sto2_8(i)=StO2(roi_index(i));
   load('sto2_9.mat')
   roi_sto2_9(i)=StO2(roi_index(i));
end
mean_sto2(1)=mean(roi_sto2_7);
mean_sto2(2)=mean(roi_sto2_8);
mean_sto2(3)=mean(roi_sto2_9);

min_sto2(1)=min(roi_sto2_7);
min_sto2(2)=min(roi_sto2_8);
min_sto2(3)=min(roi_sto2_9);

max_sto2(1)=max(roi_sto2_7);
max_sto2(2)=max(roi_sto2_8);
max_sto2(3)=max(roi_sto2_9);
figure; subplot(1,3,1);  bar(min_sto2);ylim([0 100]);
title('Min StO2 in ROI (without prior)');
subplot(1,3,2); bar(max_sto2);ylim([0 100]);
title('Max StO2 in ROI (without prior)');
subplot(1,3,3);  bar(mean_sto2);ylim([0 100]);
title('average StO2 in ROI (without prior)');
```

VITA

Dhanashree Palande

Candidate for the Degree of

Master of Science

Thesis: TRANS-RECTAL OPTICAL TOMOGRAPHY RECONSTRUCTION USING 3-DIMENSIONAL SPATIAL PRIOR EXTRACTED FROM SPARSE 2-DIMENSIONAL TRANS-RECTAL ULTRASOUND IMAGERY

Major Field: Electrical Engineering

Biographical:

Personal Data: Pune, Maharashtra, India on November 25, 1988

Education:

Completed the requirements for the Master of Science in Electrical Engineering at Oklahoma State University, Stillwater, Oklahoma in July, 2013.

Completed the requirements for the Bachelor of Engineering in Electronics and Telecommunication at University of Pune, Pune, Maharashtra, India in 2010.

Experience:

Worked as Research Assistant at Optical Imaging Lab at Oklahoma State University with Dr. Daqing Piao from August 2012 to July 2013.

Worked as Programmer Analyst Trainee at Cognizant Technology Solutions, India from September 2010 to July 2011.